Highlights

Cyclomap: A new phase-cycle analysis to study the kinematics of gears and bearings.

Thato Sibanda, Stephan Schmidt

- A new phase-cycle analysis named cyclomap is proposed for gear and bearing diagnostics.
- The behaviour of the damaged bearing's repetitive transients can be observed under different conditions.
- Demonstrated the phase modulations of gear and bearing signals that impede damage detection.

Cyclomap: A new phase-cycle analysis to study the kinematics of gears and bearings.

Thato Sibanda[a,*], Stephan Schmidt[a]

[a]*Centre for Asset Integrity Management, Department of Mechanical and Aeronautical Engineering, University of Pretoria, Pretoria, South Africa*

Abstract

The object of this paper is to propose a new phase-cycle analysis for gear and bearing diagnostics of rotating machinery which synthesises the theory of *angle-time cyclostationary* (AT-CS). The motivation for this research came from bearing diagnostics which is confronted by the inevitable smearing phenomenon due to bearing slip. The bearing signal under non-stationary conditions is neither jointly *second-order cyclostationary* (CS2) nor *pseudo-cyclostationary* (pseudo-CS) and, hence, most CS2 tools are subjected to loss of diagnostics information. The proposed phase-cycle analysis is believed to propound the study of the kinematics of gears and bearings, and it will significantly modify the prevailing historical interpretation of the bearing slip. In this paper, the phase-cycle analysis which is based on the theory of AT-CS is named the "cyclomap" because it can provide much more information about the kinematics of cyclostationary and cyclo-non-stationary signals. The cyclomap shows some interesting features in delineating the energy distribution of the kinematical properties of machines at an angular period of interest. In order to further study the properties of the cyclomap, it is systematically compared to the well-known order-frequency cyclic modulation coherence in diagnosing the CS2, pseudo-CS, and second-order cyclo-non-stationary signals of the experimental datasets.

Keywords: Cyclomap, Phase-cycle analysis, Gear diagnostics, Bearing diagnostics, Time-varying operating conditions, Bearing slip

1. Introduction

Vibration-based condition monitoring has been proven effective in the detection and diagnosis of gear and bearing faults in order to increase the operational availability of many types of rotating machinery [1, 2]. If vibration signals of rotating machinery exhibit *second-order cyclostationary* (CS2) then many signal processing techniques can be exploited [3]. An impetus to the use of signal processing techniques has undoubtedly improved the detection of gear and bearing faults. Conventional techniques, such as the *squared envelope spectrum* (SES), *enhanced envelope spectrum* (EES), and *improved envelope spectrum* (IES), are well established and have proved to be very effective in machinery diagnostics [4–6].

The problem of detecting the hidden cyclic periodicities in mechanical signals generated by a variety of rotating machinery has a very long history [7, 8]. In the literature, the problem of detecting hidden periodicities is one of great difficulty and one which has attracted the attention of most of the great meteorologists, mathematicians, astronomers, and physicists for some 140 years. Among early researchers is the distinguished Fellow of the Royal Society, Schuster, and Rayleigh [9]. Schuster was keenly interested in the mathematical theory of periodicities and devised a new method called the *periodogram* [10] in 1898, in a memoir entitled "On the investigation of hidden periodicities with application to a supposed 26 day period of meteorological phenomena.", that has so long remained unpublished in the archives of the Royal Society. The periodogram as an estimate of the spectral density function of a stationary time series has been very largely used in subsequent work when periods have been investigated in the science of meteorology [11, 12]. At the end of the nineteenth century, and the beginning of the twentieth century, the periodogram analysis attracted the attention of many researchers, not least in physics, engineering, and mathematics, extending even into economics [13–16]. The most basic purpose of the periodogram is to represent a time series by a sum of weighted sinusoidal functions called *spectral components*. The spectral window or kernel in the decomposition of a signal into spectral components is called the *spectral density*. This spectral density is equivalent to the spectrum of the time series [17–24]. In particular, the concept of the spectral window was introduced by Blackman and Tukey [19, 20]. After some time, the periodogram was found to give a misleading result which has led to attempts to find more efficient methods. About 1945-46, Bartlett [25] and Daniell pointed out that the periodogram needs to be smoothed if it is to form a consistent estimate of the spectral density function. Daniell also suggested in 1946 that averaging the periodogram over neighbouring frequencies could increase the stability of the estimate of the spectral density. In the early 1950s,

Abbreviations: ACP, averaged cyclic periodogram; AF-IPS, angle-frequency instantaneous power spectrum; AT-CS, angle-time cyclostationary; AT-IPS, angle-time instantaneous power spectrum; CNS, cyclo-non-stationary; CNS2, second-order cyclo-non-stationary; CPW, cepstrum pre-whitening; CS, cyclostationary; CS2, second-order cyclostationary; CSD, cyclic spectral density; DFT, discrete Fourier transform; EES, enhanced envelope spectrum; FFT, fast Fourier transform; HFRT, high-frequency resonance technique; IES, improved envelope spectrum; OFCMCoh, order-frequency cyclic modulation coherence; SC, spectral correlation; SCP, smoothed cyclic periodogram; SES, squared envelope spectrum; STFT, short-time Fourier transform; TF-IPS, time-frequency instantaneous power spectrum

*Corresponding author.

Email address: matssibanda@gmail.com (Thato Sibanda)

Nomenclature

Operators

$\log(\cdot)$	Natural logarithm
$\mathcal{F}\{\cdot\}$	Discrete Fourier transform
$\mathcal{F}^{-1}\{\cdot\}$	Inverse discrete Fourier transform
$\|\|_{n=0}^{N-1}$	Synchronous window transform
$\|\|w\|\|^2$	Euclidean norm of w
$COT_{\Delta t\to\Delta\varphi}\{\cdot\}$	Computed order tracking transform

Variables

α	Cyclic order variable
ϕ	Angular period
τ	Time-lag variable
θ	shaft revolution variable
φ	Angular position variable
f	Spectral frequency variable
t	Time variable

Symbols

$\Delta\tau$	Time-lag resolution
$\Delta\theta$	shaft revolution resolution
$\Delta\vartheta_{rev}^{(min)}$	Minimum angular speed difference
Δ_f	Sampling frequency
Δ_t	Sampling period
Δf	Spectral frequency resolution
τ_s	s-th discrete time-lag variable
θ_n	n-th discrete shaft revolution variable
φ_a	a-th discrete angular position variable
φ_c	c-th discrete angular position variable
$\vartheta[n]$	Instantaneous angular speed
$\vartheta_{rev}[n]$	Revolutions (integrated speed)
f_k	k-th discrete spectral frequency variable
N_w	Window length
R	Hop size
R_o	Overlap fraction
t_m	m-th discrete time variable
$w[n]$	N_w-long tapering data window

Estimators

$\varepsilon_x(\varphi_c;\tau_s,\Delta\tau)$	Angle-time instantaneous power spectrum
$\varepsilon_x(\varphi_c;f_k,\Delta f)$	Angle-frequency instantaneous power spectrum
$\varepsilon_x(t_m;f_k,\Delta f)$	Time-frequency instantaneous power spectrum
$\varepsilon_x^{\phi;\Delta\tau}(\varphi_a;\theta_n,\Delta\theta)$	AT-IPS-based estimator of the cyclomap
$\varepsilon_x^{\phi;\Delta f}(\varphi_a;\theta_n,\Delta\theta)$	AF-IPS-based estimator of the cyclomap

Acronyms

BPOI	Ball Pass Order of the Inner race
BPOO	Ball Pass Order of the Outer race
BSO	Ball Spin Order
FTO	Fundamental Train Order

the *smoothed periodogram* came to the fore, and periodogram fell into disfavour [25–28]. In the subsequent years, several consistent estimates of the spectral density function were proposed which include the *averaged periodogram* [29, 30].

Gardner, who extensively researched the *spectral correlation* (SC) theory of cyclostationary time-series [31], wrote various papers, extending over some thirty-one years (1975-2006). Gardner was one of the pioneers in the latter half of the twentieth century. In 1985-87, Gardner developed the SC which is essentially the *cyclic spectral density* (CSD) estimator based on the *smoothed cyclic periodogram* (SCP) [31–34], and also to explain the extremely valuable theory of cyclostationarity [35]. It is now almost forty years since the origin of the SC. The SC decomposes a time series into a bi-spectral plane of two frequency variables with different physical meanings, namely the spectral frequency (denoted by f) and the cyclic frequency (denoted by α). This approach is undoubtedly of great power and of much utility for cases where there are underlying periodicities. Research specifically dealing with the cyclostationarity aspects of communication signals dates from the late 1950s [36]. The term *cyclostationary* (CS) was introduced by Bennett [37] in 1958 to describe random processes possessing periodically time-variant mean and auto-correlation functions. Since then, CS analysis has proved its interest in many fields like gear and bearing diagnostics. In 1999, Capdessus *et al.* [38] introduces the theory of CS processes as a powerful tool for the diagnostics of rotating machines. Moreover, the authors have demonstrated that the vibration signals measured on gear systems display *second-order cyclostationary* (CS2).

The twenty-first century had begun very promisingly for many researchers, with the work of Gardner [31] on the method of SC and the work of Welch [30] on the method of averaged periodogram (hereinafter referred to as the Welch estimator). Boustany and Antoni proposed the *averaged cyclic periodogram* (ACP) [39, 40]. The ACP finds its precursors in the CSD estimator based on the SCP and also the Welch estimator. In particular, the ACP was indubitably more flexible, as it was associated with low computational costs as compared to SC because of the Welch estimator that is powered by the *fast Fourier transform* (FFT). Cooley and Tukey stated in their original paper [22] that the FFT algorithm is formally most efficient when the number of samples in a record can be expressed as a power of 2 (i.e., $N = 2^n$, where n is an integer). In the literature, the FFT became a numerically efficient algorithm for computation of the *discrete Fourier transform* (DFT) and its inverse. As a matter of fact, the problem of detecting hidden cyclic periodicities motivated the earliest work in the development of spectral analysis and provided much of the impetus for developing the FFT. In the past few years, the appropriate tool for periodicity detection under non-stationary conditions was order-frequency analyses. The order-frequency analysis of machine signals has been extensively treated by Abboud and Antoni in this seminal

paper [41], in which the authors compared the *order-frequency cyclic modulation coherence* (OFCMCoh) with the *order-frequency averaged cyclic coherence* (OFACCoh). These tools which describe the signals in the order-frequency domain have proved to be very effective in machinery diagnostics of *cyclo-non-stationary* (CNS) signals. In addition, the authors have made enormous strides of progress in the theory of the *angle-time cyclostationary* (AT-CS). The reason for representing a vibration signal by an estimate of the CSD is that it can be efficient, and convenient, and often reveals a description of the vibration signal.

To date, Schuster's periodogram and its variant (i.e., order-frequency analyses) are often used to disclose hidden cyclic periodicities of gear and bearing faults [41–43]. However, it is imperative to consider the limitation of these tools, especially the order-frequency analyses in bearing diagnostics. In the cases of bearing diagnostics where the bearing fault signal loses periodicity due to bearing slip [3, 44, 45], the order-frequency analyses lose effectiveness due to the inevitable smearing phenomenon that results in the loss of diagnostic information. The origin of the bearing slip may be traced to the pioneering work of Broderick *et al.* [46] in 1972. Thenceforth, various ideas have been published concerning the nature of the bearing slip of the rolling element bearings [3, 44, 47–49], and the more recent investigations of the subject have been concerned with how it manifests itself under a variety of operating conditions. These papers can best be described as a guided tour through the history of spectrum estimation, starting with the *high-frequency resonance technique* (HFRT) [50] which is now called the *envelope analysis* and leading up to the order-frequency analyses. The damage bearing's repetitive transients [51] lose periodicity in the presence of slip, which deteriorates common tools for bearing diagnostics. In the literature, the bearing slip has been shown to affect most advanced CS2 tools including the *averaged instantaneous power spectrum* (AIPS) [52, 53]. Recently, Marsick *et al.* [54] introduced as method for restoring cyclostationarity of rolling element bearing signals using the concept of *cycle of reference*. According to our knowledge, the kinematical properties of gears and bearings under a variety of operating conditions have not been addressed in the literature.

In this paper, a new phase-cycle analysis method which is an extension of the *instantaneous power spectrum* (IPS) within the AT-CS framework is developed for the diagnostic practice of gears and bearings under various operating conditions. The phase-cycle analysis allow us to uncover the underlying periodicities and understand the impact of slip on the kinematics. In this paper, the phase-cycle analysis is named the *cyclomap* because it can provide much more information about the kinematics of CS and CNS signals. The cyclomap is systematically compared to the well-known OFCMCoh in diagnosing the CS2, pseudo-CS, and second-order cyclo-non-stationary (CNS2) signals of the experimental datasets.

The organization of the paper is as follows: Section 2 gives essential preliminaries. Section 3 illustrates the concept of phase-cycle analysis for a prominent description of machine kinematics. Then, we introduce a class of estimates of the phase-cycle analysis together with the mathematical foundation and flow diagram. Section 4 access the performance of the phase-cycle analysis on the IMS (Intelligent Maintenance Systems) and C-AIM (Centre for Asset Integrity Management) experimental datasets in diagnosing bearing outer/inner race and localised gear faults respectively. Section 5 conclude studies conducted in this paper.

2. Preliminaries

2.1. The angle-frequency instantaneous power spectrum

Let $\{x[n]\}_{n=0}^{L_t-1}$ be a discrete record of finite length L_t acquired at the sampling period Δ_t (or sampling frequency Δ_f), having an instantaneous angular speed $\{\vartheta[n]\}_{n=0}^{L_t-1}$ of unit [rad/s]. A precise estimation of the instantaneous angular speed can be obtained through the zebra-tape shaft encoder or tacholess instantaneous speed estimation methods [55–57]. The *short-time Fourier transform* (STFT) transforms a discrete record of finite length into two-dimensional data, with one axis as the location of the tapering data window and the second axis as the corresponding spectral frequency. The spectral frequency resolution Δf is governed by the uncertainty principle, i.e., inversely proportional to the length of each N_w-long segment. On the other hand, the time resolution Δt is a representation of a *temporal axis*: its resolution is not known *à priori* since it depends on L_t, N_w, and is inversely proportional to overlap fraction R_o. In this work, the resolution of variables that represent the temporal axis is not shown in the mathematical expression. Mathematically, the computation of the STFT using segmentation of a discrete record of finite length is expressed as

$$x(t_m; f_k, \Delta f) = \sum_{n=0}^{N_w-1} x[n + mR] \cdot w[n] e^{-2\pi i n k / N_w} \tag{1}$$

where $\Delta f = \Delta_f / N_w$ is the spectral frequency resolution or the bandwidth. The hop size R is calculated as an integer of $(1 - R_o)N_w$, where N_w is the window length and $R_o (0 < R_o \leq 1)$ is the overlap fraction, $i = \sqrt{-1}$ is an imaginary number, $\{x[n + mR]\}_{n=0}^{N_w-1}$ is the shifted version by R sample such that it selects N_w-long segment of $\{x[n]\}_{n=0}^{L_t-1}$, and $\{w[n]\}_{n=0}^{N_w-1}$ is a positive-definite N_w-long tapering data window computed from a lag-window (i.e., symmetric about zero). For the STFT to be invertible, it was recommended in Ref. [58] to take at least 75% overlapping Hanning window. Hence, the overlap fraction of $R_o \geq 0.75$ and Hanning tapering data window were used for the proposed approach. The Hanning lag-window is represented mathematically by the following equation, viz:

$$w[n] = \frac{1}{2}\Big(1 + \cos\frac{\pi n}{N_w}\Big) \tag{2}$$

where $n\ \{2N_w/(N_w-1) \mid n \in [-N_w, N_w]\}$, denote a closed interval of the set of all real numbers greater or equal to $-N_w$ and less or equal to N_w with increments of $2N_w/(N_w-1)$. In general, the complex exponential Fourier series and the sine-cosine Fourier series [59] are interrelated by the following equation, $e^{2\pi i/N} = \cos(2\pi/N) + i\sin(2\pi/N)$. The *time-frequency instantaneous power spectrum* (TF-IPS) originally developed by Page [60] in 1952, can be estimated by the normalised squared envelope of the complex envelope denoted as

$$\varepsilon_x(t_m; f_k, \Delta f) = \frac{\Delta_t}{L_t \|w\|^2} |x(t_m; f_k, \Delta f)|^2 \tag{3}$$

The scale factor introduced by Welch in Ref. [30] is dependent on the lag-window can be written as the Euclidean norm, denoted as $\|w\|^2 = \sum_{n=0}^{N_w-1} |w[n]|^2$. In order to compensate for phase modulations introduced by a non-stationary regime, the *angle-frequency instantaneous power spectrum* (AF-IPS) can be calculated by order tracking the TF-IPS with respect to the temporal (time) axis, denoted as

$$\varepsilon_x(\varphi_c; f_k, \Delta f) = COT_{\Delta t \to \Delta\varphi}\{\varepsilon_x(t_m; f_k, \Delta f)\} \tag{4}$$

where $COT_{\Delta t \to \Delta\varphi}\{\cdot\}$ is the computed order tracking transform that converts the time variable t_m at different spectral frequency f_k to an angle variable φ_c that represents a temporal (angle) axis. Let $f_k = k\Delta f$ denotes the discrete spectral frequency axis with a resolution of $\Delta f = \Delta_f/N_w$. Hence, the Nyquist frequency f_N is calculated as a product of a spectral frequency resolution and its length is denoted as $f_N = \Delta_f/N_w \times N_w/2 = \Delta_f/2$.

2.2. The angle-time instantaneous power spectrum

The extension of the AF-IPS has a variety of uses (e.g. OFCMCoh), especially in fault diagnostics of gears and bearings under a non-stationary regime. In this work, it is extended to *angle-time instantaneous power spectrum* (AT-IPS) by applying the inverse discrete Fourier transform (IDFT) with respect to the spectral frequency variable, denoted as

$$\varepsilon_x(\varphi_c; \tau_s, \Delta\tau) = IDFT_{\Delta f \to \Delta\tau}\{\varepsilon_x(\varphi_c; f_k, \Delta f)\} \tag{5}$$

An important property that makes the IDFT so eminently useful is the fact that it can be efficiently calculated by inverse fast Fourier transform (IFFT). In this case, we can rewrite Eq. (5) without loss of generality as

$$\varepsilon_x(\varphi_c; \tau_s, \Delta\tau) = \frac{1}{N_w} \sum_{k=0}^{N_w-1} \varepsilon_x(\varphi_c; f_k, \Delta f) e^{2\pi i k s/N_w} \tag{6}$$

Let $\tau_s = s\Delta\tau$ denotes the discrete time-lag axis with a resolution of $\Delta\tau = \Delta_t$. Hence, the Nyquist time-lag τ_N is calculated as a product of a time-lag resolution and its length is denoted as $\tau_N = \Delta_t \times N_w/2 = \Delta_t N_w/2$.

3. Proposed phase-cycle analysis

The object of this section is to introduce the proposed phase-cycle analysis for gear and bearing diagnostics. The phase-cycle analysis is the extension of the angle-time instantaneous power spectrum introduced in this paper. This section has three basic purposes: first is to illustrate the concept of phase-cycle analysis; second is to establish a firm mathematical foundation for a phase-cycle analysis; third is to provide a general point of view of the gear and bearing diagnostics of many types of rotating machinery.

3.1. Concept of phase-cycle analysis

This section has been prepared primarily as an expository and tutorial on the concept of phase-cycle analysis for studying machine kinematics and to cast light on its physical interpretation and to facilitate its use. In cyclostationarity paradigm, the extension of the AF-IPS has a variety of uses, especially in gear and bearing diagnostics. The extensions of angle-dependent modulations of the AF-IPS are displayed in Fig. 1. The average of the AF-IPS extensions over the whole spectral frequency f variable yields more detailed information related to machine kinematics, and, thus, offers a framework to analyse angle-dependent modulations for diagnostic purposes. In this paper, we contribute to this research direction by introducing the phase-cycle analysis.

The easiest way to demonstrate the concept of phase-cycle analysis is to use a synthetic gearbox signal with a bearing outer race fault. The phase-cycle analysis with Ball Pass Order of the Outer race (BPOO) of 8 orders of the shaft speed is presented below. It has been assumed that a full cycle (i.e. $\alpha_{BPOO}^{-1} = 1/8$ rev) corresponds to 2π radians. In bearing diagnostics, the BPOO and Ball Pass

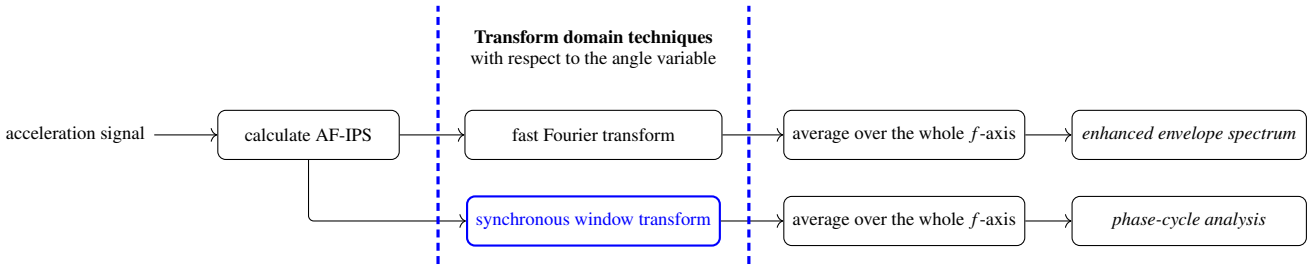

Figure 1: Flowchart for extensions of angle-dependent modulations of the instantaneous power spectrum.

Order of the Inner race (BPOI) imply the number of rolling elements that collided with a defect (i.e. outer/inner race fault) in one shaft revolution. Hence, the angular position is simply an angular portion of a BPOO/I period. The phase-cycle analysis for bearing outer race fault is presented in Fig. 2.

The shaft revolution's length L_θ is equivalent to a number of cycles (or repetitive transients) at an angular period of interest. The angular position's length L_φ is equivalent to a number of points within a cycle. It is noteworthy that the shaft revolution resolution $\Delta\theta$ corresponds to an angular period ϕ because a full cycle corresponds to 2π radians. In this paper, the phase-cycle analysis is used to study the kinematical properties of gears and bearings under a variety of operating conditions.

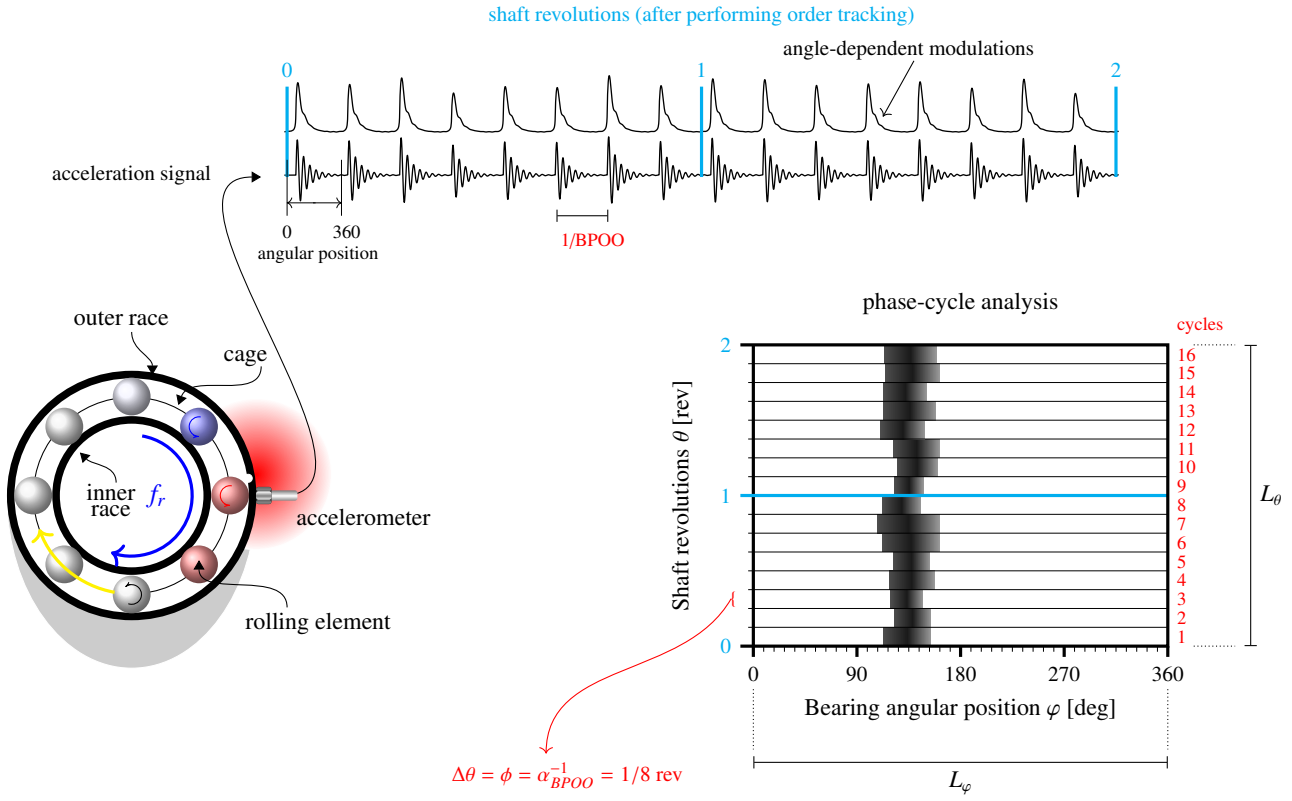

Figure 2: Illustration of the concept of phase-cycle analysis for outer race fault with 16 cycles, occurring at an angular period of $\phi = \alpha_{BPOO}^{-1} = 1/8$ rev.

3.2. The mathematical framework of phase-cycle analysis

The object of this section is to provide a comprehensive view of phase-cycle analysis within the AT-CS framework. Before approaching the development of the necessary tools, we first introduce synchronous window transform for extending AT-IPS into three dimensions. The synchronous window transform makes it possible to obtain a three-dimensional generalisation of the AT-IPS (or AF-IPS) that can be exploited to represent the phase-cycle behaviour of the repetitive transients, which describe the health of rotating machinery. Hence, the phase-cycle estimator which delineates a vibration signal in a bivariate angular referential can provide insights into the kinematical properties of CS and CNS signals both in terms of angular position (denoted by φ) and the shaft

revolutions (denoted by θ), thus describing the kinematics of gears and bearings (i.e. the behaviour of bearing slip). The synchronous window transform consists of slicing the angle-dependent modulations at an angular period ϕ of interest and concatenating the cycles at a resolution of $\Delta\theta$. To give mathematical expression to this, let us define three-dimensional AT-IPS as

$$\varepsilon_x^{\phi}(\varphi_a;\tau_s,\Delta\tau;\theta_n,\Delta\theta) = \Big\|_{n=0}^{L_\theta-1} \varepsilon_x(\varphi_a + n\cdot L_\varphi;\tau_s,\Delta\tau), \tag{7}$$

where $\|_{n=0}^{L_\theta-1}\cdot$ denotes the synchronous window transform performed over the whole length of the signal, $\varphi_a = a\Delta\varphi$ is an angular position which represents a temporal (phase angle) axis, L_φ is the angular length of the chosen angular period, and n is the number of shifting operations which are used to slice the segments or synchronous signals on the AT-IPS, $\varepsilon_x(\varphi_c;\tau_s,\Delta\tau)$. Let $\theta_n = n\Delta\theta$ denotes the discrete shaft revolutions axis with a resolution of $\Delta\theta = \phi = \alpha_{fault}^{-1}$, where α_{fault} denotes the characteristic cyclic orders α of the gear or bearing fault. As demonstrated in Section 3.1, it has been assumed that a full cycle (i.e. $\phi = \alpha_{fault}^{-1}$ of units [rev]) is equivalent to 2π radians. Hence, the angular period ϕ is the only parameter that controls the shaft revolutions resolution $\Delta\theta$. In order to arrive at three-dimensional AT-IPS, $\varepsilon_x^{\phi}(\varphi_a;\tau_s,\Delta\tau;\theta_n,\Delta\theta)$, we just concatenate the AT-IPS using the synchronous window transform. The phase-cycle analysis for discrete-time variable equals the summation of the three-dimensional AT-IPS with respect to the time-lag variable, viz:

$$\varepsilon_x^{\phi;\Delta\tau}(\varphi_a;\theta_n,\Delta\theta) = \frac{2}{N_w+2}\sum_{s=0}^{N_w/2}\varepsilon_x^{\phi}(\varphi_a;\tau_s,\Delta\tau;\theta_n,\Delta\theta), \tag{8}$$

where $\varepsilon_x^{\phi;\Delta\tau}(\varphi_a;\theta_n,\Delta\theta)$ is the phase-cycle analysis estimator, henceforth called the *cyclomap*, which is based on the three-dimensional AT-IPS. In particular, the AT-IPS-based cyclomap aims to extract all diagnostic information to quantify machine health conditions. Likewise, the AF-IPS-based cyclomap, $\varepsilon_x^{\phi;\Delta f}(\varphi_a;\theta_n,\Delta\theta)$, can be written as discrete-frequency variable, denoted as

$$\varepsilon_x^{\phi;\Delta f}(\varphi_a;\theta_n,\Delta\theta) = \frac{2}{N_w+2}\sum_{k=0}^{N_w/2}\varepsilon_x^{\phi}(\varphi_a;f_k,\Delta f;\theta_n,\Delta\theta), \tag{9}$$

According to Parseval's theorem [61], the total energy computed in the angle-time autocorrelation function must equal the total energy computed in the AF-IPS $\sum_{k=0}^{N_w-1}\varepsilon_x(\varphi_c;f_k,\Delta f) = \sum_{k=0}^{N_w-1}|IDFT_{\Delta f\to\Delta\tau}\{\varepsilon_x(\varphi_c;f_k,\Delta f)\}|$; hence, there is a conceptual equivalence between the AT-IPS- and AF-IPS-based cyclomaps. By Eq. (8) and (9), it suffices to show that

$$\varepsilon_x^{\phi;\Delta\tau}(\varphi_a;\theta_n,\Delta\theta) = \varepsilon_x^{\phi;\Delta f}(\varphi_a;\theta_n,\Delta\theta), \tag{10}$$

If the median instead of the average is used then this equivalence is not true anymore. In this specific case, however, the AT-IPS-based cyclomap estimated using median and average statistics are still equivalent. Hence, the AF-IPS-based cyclomap will be used as a benchmark to show the performance of the AT-IPS-based cyclomap. The resulting information can provide insights into the nature of the CS and CNS signals and thus has allowed studying the kinematics of the faults. The shaft resolution's length L_θ and the angular position's length L_φ control the number of points on the cyclomap. The product of the shaft resolution's length and angular position's length denoted as $L_\varphi L_\theta$, is equivalent to the length of an angle variable φ_c on the AF-IPS or AT-IPS in Eq. (4) or (5) respectively. In the case of larger window length N_w and smaller overlap fraction R_o, the number of points on the cyclomap becomes very low. Mathematically speaking, L_φ is never a problem because L_t is usually large enough to keep a sufficient number of points. On the other hand, L_θ suffers when the angular period $\phi = \alpha_{fault}^{-1}$ approaches unity or becomes much greater than unity. This relation may be exhibited in the expanded form

$$L_\varphi L_\theta \sim \frac{L_{cot} - N_w R_o}{N_w - N_w R_o} = \frac{(1/\Delta\vartheta_{rev}^{(min)} + 1)\cdot\vartheta_{rev}[L_t - 1] - N_w R_o}{N_w - N_w R_o}, \tag{11}$$

where $\vartheta_{rev}[n] = (\sum_{n=0}^{L_t-1}\vartheta_m[n])/(2\pi\Delta_f)$, is the actual revolutions obtained by integrating the instantaneous angular speed $\{\vartheta[n]\}_{n=0}^{L_t-1}$ of unit [rad/s], $\sum_{n=0}^{L_t-1}\vartheta_m[n]$ is the cumulative sum of the instantaneous angular speed, $\Delta\vartheta_{rev}^{(min)}$ is the minimum angular speed difference, the variable $N_w R_o$ is calculated as an integer. The shaft revolution's length L_θ is calculated as an integer of $L_\theta = (\vartheta_{rev}[L_t - 1])/\Delta\theta$. The order-tracked signal length L_{cot} boils down to signal length L_t when the vibration signal is measured under constant operating conditions. The right-hand side of Eq. (11) is a function of window length N_w and overlap fraction R_o only. It will be seen that the relation between the binary logarithm of the $L_\varphi L_\theta$ and the window length N_w is linear for the range of N_w and R_o investigated. This is borne out by the results plotted as curves in Fig. 3.

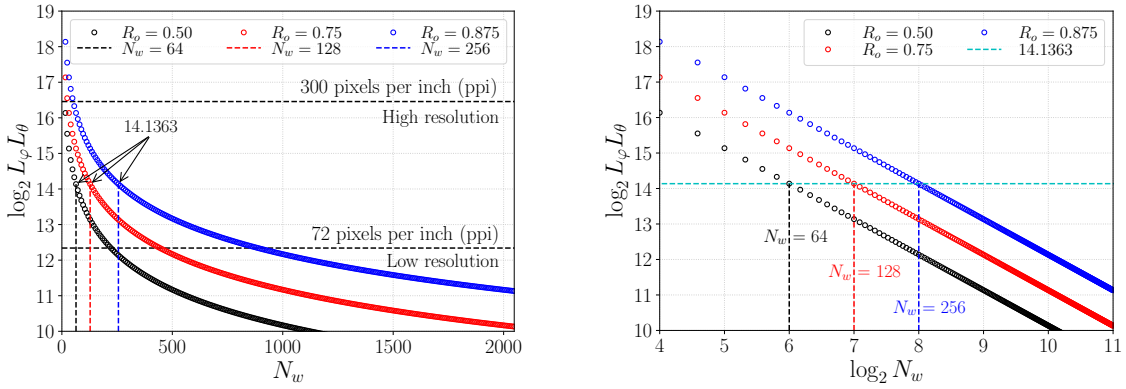

(a) (b)

Figure 3: The resolution on the cyclomap as a function of window length N_w and overlap fraction R_o.

Illustrated in Fig. 3(a) is the binary logarithm of the number of points of the cyclomap denoted as $\log_2 L_\varphi L_\theta$, as a function of the window length N_w at overlap fractions R_o of 0.50, 0.75, and 0.875. These overlap fractions should give roughly constant spacing on a binary (or natural) logarithmic scale. Nonetheless, the variation of $\log_2 L_\varphi L_\theta$ with N_w is much more pronounced than the variation with R_o. The curve given in Figs. 3(a) and 3(b) were drawn using the parameter from data obtained from the Centre for Asset Integrity Management (C-AIM) experiments which will be described in Section 4.2. The $L_\varphi L_\theta$ can also be written using the first law of logarithms denoted as $\log_2 L_\varphi L_\theta = \log_2 L_\varphi + \log_2 L_\theta$. Strictly speaking, $\log_2 L_\theta$ is a single arbitrary constant that scales the magnitude of the function since it depends on the total number of complete shaft revolutions $\vartheta_{rev}[L_t - 1]$ and the angular period $\phi = \Delta\theta = \alpha_{fault}^{-1}$ which are both parameters. On the contrary, $\log_2 L_\varphi$ is not only dependent on the window length N_w but also on the overlap fraction R_o.

The total number of points on the cyclomap scales almost as $L_\varphi L_\theta \sim 2^{14.1363}$ when the minimum angular speed difference is calculated as $\Delta\vartheta_{rev}^{(min)} = 8.063 \times 10^{-5}$, the total number of shaft revolutions is $\vartheta_{rev}[L_t - 1] = 46.4658$ rev, the window length is $N_w = 2^6$ or $N_w = 2^7$ or $N_w = 2^8$, and the overlap fraction is $R_o = 0.50$ or $R_o = 0.75$ or $R_o = 0.875$ respectively. In this case, the $L_\varphi L_\theta$ lies between the low resolution of $2^{\log_2(72^2)} = 2^{12.33985}$ and high resolution of $2^{\log_2(300^2)} = 2^{16.45764}$. In this paper, the window length and the overlap fraction will be adjusted such that the total number of points on the cyclomap fall between the low and high resolution. The two curves are shown in Fig. 3(b) which correspond to overlap fractions R_o of 0.50, 0.75, and 0.875 is diminishing approximately by successive factors of 2^1. In this case, it is much better to work with binary logarithms of window lengths instead of the window lengths themselves. The mere fact that the resolution of the cyclomap can be mathematically represented in this fashion reduced the laborious work of its computation. It is clear that the relation between the $\log_2 L_\varphi L_\theta$ and $\log_2 N_w$ is one of inverse proportionality. In particular, it can readily give useful approximations in such cases as N_w very small or very large. However, when the window length N_w gets smaller or the overlap fraction R_o approaches unity, the squared envelope of the complex envelope leads to considerable complexity and an explosion in computational cost.

3.3. Proposed methodology

The flow diagram for a phase-cycle analysis is shown in Fig. 4 and the step-by-step details for its extraction are described as follows.

Step 1. Acquire the acceleration signal and apply NAMVOC [62] to remove amplitude modulations.

Step 2. Apply the whitening procedure using the *cepstrum pre-whitening* (CPW) [63] and calculate the time-frequency instantaneous power spectrum (TF-IPS), $\varepsilon_x(t; f, \Delta f)$.

Step 3. Order track the TF-IPS, $\varepsilon_x(n; f, \Delta f)$ with respect to the time axis to yield an angle-frequency instantaneous power spectrum (AF-IPS), $\varepsilon_x(\varphi; f, \Delta f)$.

Step 4. Apply the inverse fast Fourier transform to AF-IPS, $\varepsilon_x(\varphi; f, \Delta f)$ with respect to spectral frequency axis to yield an angle-time instantaneous power spectrum (AT-IPS), $\varepsilon_x(\varphi; \tau, \Delta\tau)$.

Step 5. Apply the synchronous window to AT-IPS, $\varepsilon_x(\varphi; \tau, \Delta\tau)$ with respect to angle axis at a targeted angular period $\phi = \alpha_{fault}^{-1}$ to yield three dimensional representation called, the SW-AT-IPS, $\varepsilon_x^{\phi}(\varphi; \tau, \Delta\tau; \theta, \Delta\theta)$.

Step 6. Integrate the SW-AT-IPS with respect to the time-lag axis to yield the AT-IPS-based cyclomap, $\varepsilon_x^{\phi;\Delta\tau}(\varphi; \theta, \Delta\theta)$.

The reduction of the three-dimensional AT-IPS with median or average will therefore provide estimates of the enhanced synchronous vibration signal at an angular period of interest. The AT-IPS-based cyclomap has some interesting diagnostic properties as

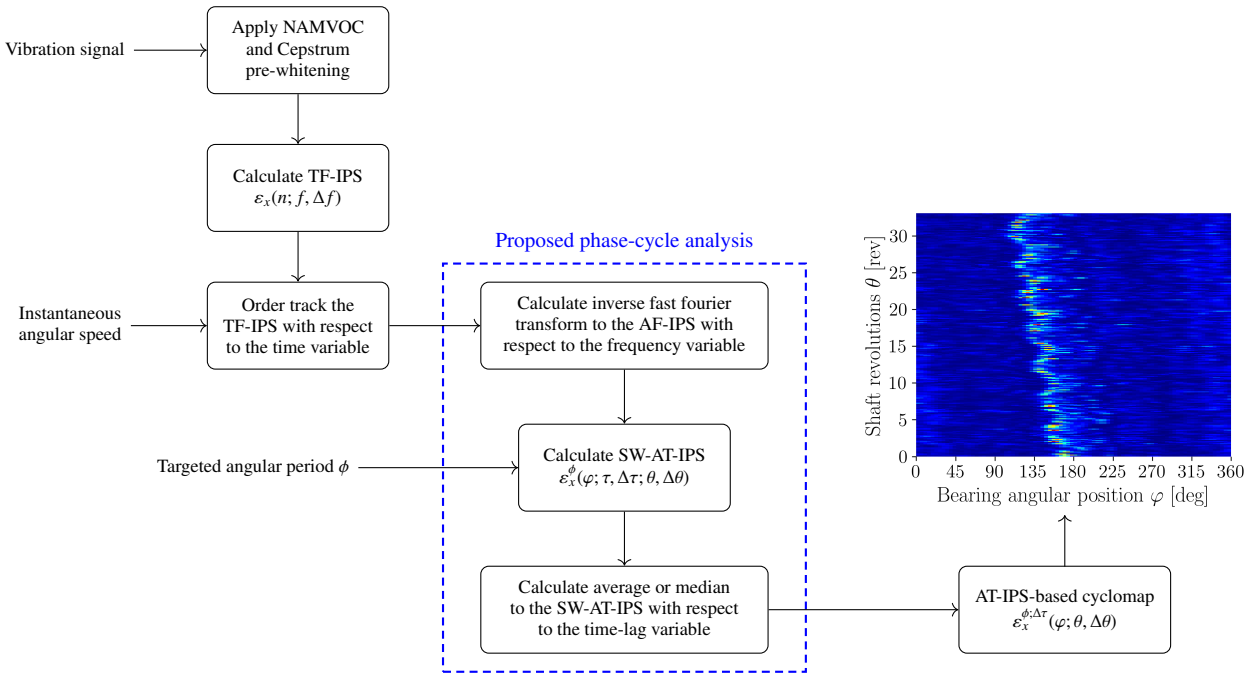

Figure 4: Flow diagram for a phase-cycle analysis.

compared to the AF-IPS-based cyclomap, and it has the advantage of great flexibility because it can be estimated using both median and average statistics. In Section 4.1.2, this will be demonstrated in more detail. The primary purpose of the cyclomap is to isolate the repetitive transients at an angular period of interest so as to enable us to study them separately.

The cyclomap as a fault diagnostic methodology permits one to identify the presence of the defect, its kind, and its location (see Fig. 4). In detail, the *presence* of the defect is identified based on the repetitive transients on the phase-cycle analysis. The *kind* of the defect can be divided into two categories namely, gear and bearing. For gear faults, the kind is limited to localised faults (i.e. tooth damage) and distributed faults (i.e. multiple teeth damage). On the other hand, the kind of bearing fault includes the outer race, inner race, rolling element, and cage fault. In particular, the shape of the repetitive transients on the phase-cycle analysis is used for this purpose. Lastly, the *location* of the defect on the component is identified based on the angular position on the gear/bearing angular position of the cyclomap.

The proposed methodology is general, with no assumption required whether it is a gear or bearing under consideration or whether it is constant or varying operating conditions. In this work, the cyclomap will be used to diagnose the bearing outer/inner race and localised gear fault. The proposed method is investigated in the next section.

4. Experimental investigations

In the previous section, we have discussed the phase-cycle analysis, but a somewhat fuller discussion on the practical side is required before an opinion of its capabilities and limitations can be formed. For this purpose, it is especially necessary to investigate the kinematics of gears and bearings under a variety of operating conditions. In this section, it is shown that the dual counterpart of the spectral frequency (i.e. the time-lag τ) is far more flexible since it provides consistently reliable means of computing the total energy using the median statistic. In Section 4.1 and 4.2, we shall assimilate the phase-cycle analysis for bearing and gear diagnostics respectively. In addition, we offer two further case studies that demonstrate its validity even more rigorously.

4.1. IMS experimental dataset

The bearing run-to-failure data provided by the Center for Intelligent Maintenance Systems (IMS) at the University of Cincinnati [64] is used as a benchmark dataset. In the accelerated bearing degradation experiment, four Rexnord ZA-2115 double-row bearings were used to support shaft rotation with a constant speed of 2000 RPM. The shaft is driven by an AC motor and coupled with rub belts. A radial load of 2721.55 kg is added to the shaft and bearing by a spring mechanism. The vibration signals were collected by four accelerometers type PCB 353B33 High Sensitivity Quartz ICPs mounted in the radial direction. All four bearings are force lubricated. An oil circulation system regulates the flow and the temperature of the lubricant. Four thermocouples were attached to the outer race of each bearing to record the bearing temperature for monitoring lubrication purposes. The IMS experimental test rig is shown in Fig. 5.

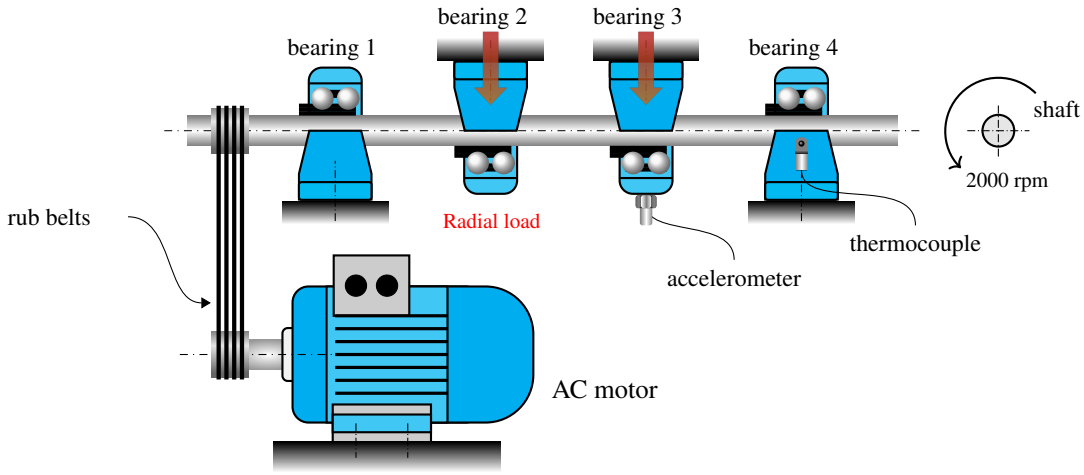

Figure 5: Intelligent Maintenance Systems (IMS) experimental test rig [64].

Vibration data was collected by a National Instruments DAQCard-6062E data acquisition card. Data collection is conducted by a National Instruments LabVIEW program. A sampling frequency of 20.480 kHz was used to sample a temporal vibration signal and store it in a file every 10 min. A file containing a vibration signal with a length of 20,480 samples was recorded. Three data sets (i.e. Set No.1, Set No.2, and Set No.3) are included in the IMS data packet. Each data set describes a test-to-failure experiment. Set No.2, and Set No.3 contained the bearing outer race fault which occurred in bearing 1 and bearing 3 respectively. Set No.1 contained the bearing inner race fault and the rolling element fault which occurred in bearing 3 and bearing 4 respectively. During the bearing run to failure process, a total of 984 files of 1 sec duration each were collected for the Set No.2. Each of the bearings in the experimental setup consists of 16 rolling elements, having a pitch diameter of 7.1501 cm, a rolling element diameter of 0.840 cm, and a tapered contact angle of 15.171 degrees. At the end of the test, an outer race fault in bearing 1 occurred after exceeding the designed lifetime (i.e. more than 100 million revolutions). Four characteristic cyclic frequencies important for bearing diagnostics are well treated by Randall and Antoni in Ref. [3]. The four theoretical characteristic cyclic orders α of the bearing outer race fault for Set No.2 are calculated as follows:

- Ball Pass Order of the Outer race (BPOO) being equal to 7.093,
- Ball Pass Order of the Inner race (BPOI) being equal to 8.907,
- Ball Spin Order (BSO) being equal to 4.201,
- Fundamental Train Order (FTO) being equal to 0.443.

It is worth recalling that the $BPFO = f_r \cdot BPOO$, with $f_r = \min\{\vartheta[n]\}/(2\pi)$ being the shaft speed in Hertz. The *orders* represent the number of cycles per shaft revolution and are thus ideal for representing speed-dependent vibrations [65–67]. In this case, the shaft frequency is directly calculated from the rotating speed as $f_r = 2000/60 = 33.33$ Hz. The product of shaft frequency and BPOO yield the bearing outer race fault frequency $BPFO = f_r \cdot BPOO = 7.093 \times 33.33 = 236.4$ Hz. For this paper, we will only work with non-dimensional characteristic cyclic orders α to accommodate the vibration signals under time-varying operating conditions. In the case of bearing fault, the cyclic orders imply the number of rolling elements that collided with a defect (i.e. inner or outer race) in one shaft revolution. The cyclic orders for gear or pinion fault reflect the number of cycles per shaft revolution. In the literature, the bearing outer race fault for Set No.2 has been extensively studied [68, 69]. Therefore, the bearing outer race fault for Set No.2 will be considered first in Section 4.1.1. Then, the bearing outer race fault for Set No.3 and the bearing inner race fault for Set No.1 is considered in Section 4.1.2 and 4.1.3 respectively. The purpose of these subsections is to gain preliminary insight into diagnosing the bearing outer/inner race fault using the cyclomap and also to study the kinematics of bearings.

4.1.1. Set No.2: bearing outer race fault (bearing 1)

The object of this section is to investigate the performance of the phase-cycle analysis on the IMS experimental datasets which will enable us to find out the kinematical properties of the bearing outer race fault, and thence the kinematical properties of the bearing slip itself. Although, the IMS experiments were mainly performed more than two decades ago, are merely of a preliminary character. There is still much scope to understand the effect of operating conditions on bearing slip. As we do not know much about the structure of the mechanical systems we can only hope to obtain rich diagnostic information using fault diagnostic techniques because they do not require exact knowledge of the kinematics of the system. The cyclomaps for measurement number 703 with BPOO of 7.08 orders of the shaft speed are presented in Fig. 6. The localised fault in a bearing such as the outer race fault under constant operating conditions is better known as the pseudo-cyclostationary (pseudo-CS) signals.

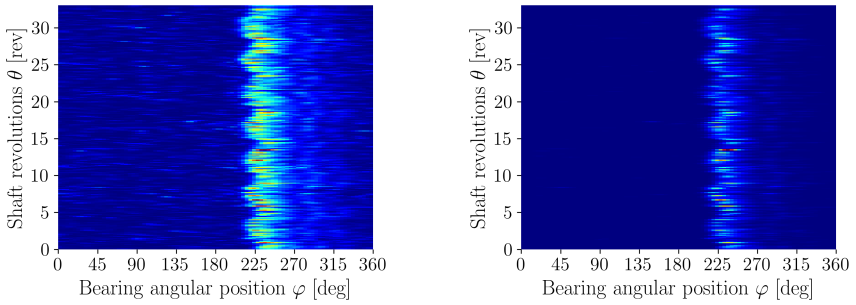

(a) (b)

Figure 6: AT-IPS-based cyclomaps, $\varepsilon_x^{\phi;\Delta\tau}(\varphi;\theta,\Delta\theta)$, for bearing outer race fault (measurement number 703) under constant operating conditions or pseudo-cyclostationary signal at a mean angular position of 229 deg, with 235 repetitive transients, occurring at an angular period of $\Delta\theta = \phi = \alpha_{BPOO}^{-1} = 1/7.08$ rev, (a) cyclomap for raw signal, and (b) cyclomap for the squared envelope of a raw signal.

In this case, the total number of points on the cyclomap scales almost as $L_\varphi L_\theta \sim 2^{14.322}$, (i.e. $\{L_\varphi; L_\theta\} = \{87; 235\}$) when the minimum angular speed difference is calculated as $\Delta\vartheta_{rev}^{(min)} = 1.628\times10^{-3}$, the total number of shaft revolutions is $\vartheta_{rev}[L_t-1] = 33.333$ rev, the window length is $N_w = 2^3$, and the overlap fraction is $R_o = 0.99$. The computational cost for these cyclomaps is still very low (i.e. about 0.4 sec) because the IMS bearing signals are very short. Since the resolution of the angular position represents the temporal axis, it will vary directly to overlap fraction. On the other hand, the shaft revolutions resolution denoted by $\Delta\theta$ will vary inversely to angular period $\phi = \alpha_{BPOO}^{-1}$. In this case, the angular period is $\phi = 1/7.08$ rev, meaning that there are 7.08 cycles (or repetitive transients) for each shaft revolutions θ. Hence, this bearing outer race fault contained 235 repetitive transients which occurred within 1 sec or approximately 33.2 shaft revolutions. Interestingly, the length of the shaft revolutions θ on the cyclomap at an angular period of interest gives us information about the total number of repetitive transients. The colours of the cyclomap are correlated with the repetitive transients. Dark blue is for minimum amplitude and dark red is for maximum amplitude.

In the smallest interval of time (i.e. 1 sec/235 = 0.00426 sec), there is a repetitive transient that is caused by the collision between the rolling element and the defect on the bearing outer race as illustrated in Figs. 6(a) and 6(b). The very striking result, even at first sight startling, is the behaviour of the repetitive transients for bearing outer race fault. It has long been known for many decades that the bearings experience a random slip, but a closer examination of the repetitive transients somewhat weakens the argument that the bearing slip is random. The behaviour of the damaged bearing's repetitive transients will be further investigated in Section 4.1.2. In particular, a signal is said to be random if and only if the behaviour is unpredictable in such a way that its future is entirely independent of its past. Loosely speaking, this deterministic trajectory of the repetitive transients has been found to fit the behaviour of cage modulation [51, 68, 70] to a remarkable degree. Hence, this kinematical property leaves us then with a certain amount of doubt as to the correct behaviour of the bearing slip. Further investigations may be necessary to explain the conditions requisite for the kinds of motions or kinematical properties with which the bearing slip is expected to be endowed.

4.1.2. Set No.3: bearing outer race fault (bearing 3)

The kinematical properties of the bearing slip's behaviour are further investigated in this section. The purpose of this section is to also highlight the benefits of using the AT-IPS-based cyclomap instead of the AF-IPS-based cyclomap. The AF-IPS-based cyclomap provides the required information directly, but its performance can be impeded by spectral frequency content. Therefore, the purpose of this section is to show the benefits of the AT-IPS-based cyclomap over the AF-IPS-based cyclomap. The methods will be compared in the present and the ensuing subsection. The AF-IPS-based cyclomap and AT-IPS-based cyclomap for measurement number 6316 with BPOO of 7.10 orders of the shaft speed are presented in Fig. 7.

The bearing outer race fault is very prominent in both figures. The angular position variable is perhaps the most interesting and potentially the most useful variable since it presents richer diagnostic information related to the phase angle of each repetitive transient. On the cyclomap there are 7.10 cycles for each shaft revolutions θ. Hence, this bearing outer race fault has 236 repetitive transients which occurred in 1 sec or approximately 33.2 shaft revolutions. The AF-IPS and AT-IPS-based cyclomaps are presented in Figs. 7(a) and 7(b) as a demonstration of the superiority of the latter over the former. When the median statistic is used to compute the total energy, we advocate the use of AT-IPS-based cyclomap because it provides a significantly higher SNR as compared to the AF-IPS-based cyclomap. This property makes the former an attractive diagnostic tool and thus a competitor to the latter.

The kinematical properties of the bearing outer race fault in Fig. 7(b) and Fig. 6(b) are in good agreement. The fact that the line is tilted is obviously due to the uncertainty of the estimated fault period. As a matter of fact, no precise determination of shaft speed exists, except in cases where it is indefinitely slow. The fact that the damaged bearing's repetitive transients lose periodicity in the presence of slip, which deteriorates common tools for bearing diagnostics is a fact that was recognised by the earliest researchers.

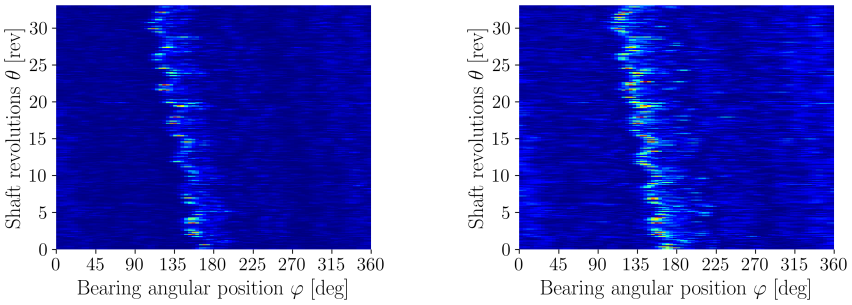

(a) AF-IPS-based cyclomap (b) AT-IPS-based cyclomap

Figure 7: Bearing outer race fault (measurement number 6316) representing pseudo-cyclostationary signal at a mean angular position of 150 deg, with 236 repetitive transients, occurring at an angular period of $\Delta\theta = \phi = \alpha_{BPOO}^{-1} = 1/7.10$ rev, (a) AF-IPS-based cyclomap, $\mathcal{E}_x^{\phi;\Delta f}(\varphi;\theta,\Delta\theta)$, reflecting spectral density information, and (b) AT-IPS-based cyclomap, $\mathcal{E}_x^{\phi;\Delta\tau}(\varphi;\theta,\Delta\theta)$, reflecting spectral components information.

From the preceding results, we may conclude *à fortiori* that a periodic cage modulation at an angular period of $\phi = \alpha_{FTO}^{-1}$ is more pronounced as compared to the actual random slip because it introduces substantially large phase modulations. Small discrepancies in the repetitive transients may be due to actual random slip, or estimation errors due to the order tracking technique. Further investigations need to be performed to investigate whether the actual random slip contributes minimally to the smearing phenomenon or whether there are other factors (such as cage modulation) that control its appearance.

4.1.3. Set No.1: bearing inner race fault (bearing 3)

The benefits of using the AT-IPS-based cyclomap instead of the AF-IPS-based cyclomap are further investigated in this section. The purpose of this section is to gain preliminary insight into diagnosing the bearing inner race fault. The AF-IPS-based cyclomap and AT-IPS-based cyclomap for measurement number 2156 with BPOI of 2.02 orders of the shaft speed are presented in Fig. 8. In this case, the total number of points on the cyclomap scales almost as $L_\varphi L_\theta \sim 2^{14.322}$, (i.e. $\{L_\varphi; L_\theta\} = \{305; 67\}$).

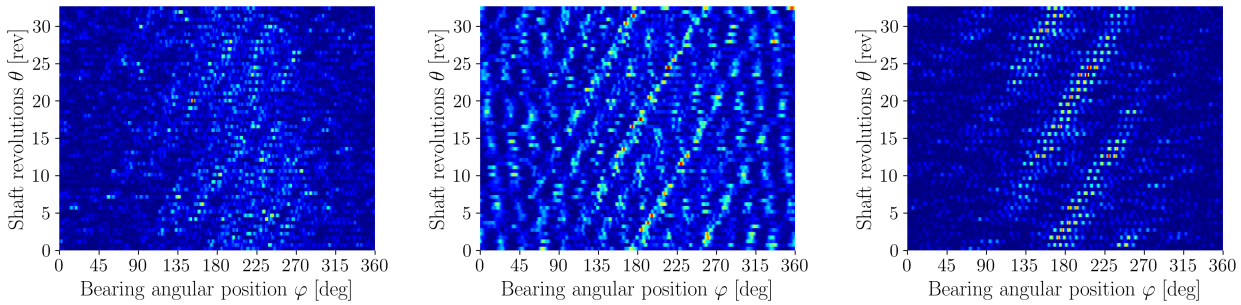

(a) AF-IPS-based cyclomap (b) AT-IPS-based cyclomap (c) AT-IPS-based cyclomap (filtered)

Figure 8: Bearing inner race fault (measurement number 2156) representing pseudo-cyclostationary signal, occurring at an angular period of $\Delta\theta = \phi = \alpha_{BPOI}^{-1} = 1/2.02$ rev, (a) AF-IPS-based cyclomap, $\mathcal{E}_x^{\phi;\Delta f}(\varphi;\theta,\Delta\theta)$, (b) AT-IPS-based cyclomap, $\mathcal{E}_x^{\phi;\Delta\tau}(\varphi;\theta,\Delta\theta)$, and (c) AT-IPS-based cyclomap for filtered signal.

Illustrated in Fig. 8(a) is the AF-IPS-based cyclomap which offer at least some speculative insights into the kinematical properties of the bearing inner race fault. However, the results clearly show a loss of diagnostic information when the total energy is computed using the median statistic instead of averaging. On the other hand, the AT-IPS-based cyclomap in Fig. 8(b) shows some evidence of the inner race fault. Hence, the conceptual equivalence between the AT-IPS- and AF-IPS-based cyclomaps, however, breaks down in this specific case. But, the potential insights to be gained from the AT-IPS-based cyclomap are lost because they are clouded by low-frequency components. In such cases, it may be desirable to institute an investigation to ascertain the reason for the aberrant behaviour of the bearing inner race fault.

The way out of this impasse requires filtering to remove low-frequency non-modulating signals. Hence, the cyclomap for a filtered signal presented in Fig. 8(c) provides a significantly better signature that comprises obvious repetitive transients around 200 deg. It is noteworthy that the pre-whitening was not used because it removed all diagnostic information. By virtue of its flexibility, pre-whitening (we shall say more about this in Section 4.2.1) plays a significant role in fault diagnostics since it covers a wide enough range of cases in practice to have rather broad utility. To conclude, the signature of the bearing outer/inner race faults are most apparent and are very important, both kinematically and also from the bearing diagnostic point of view.

4.1.4. OFCMCoh: Enhanced envelope spectrum

The order-frequency analysis is well established and has proved to be very effective in revealing hidden cyclic periodicities embedded in strong environmental noise. In this section, the order-frequency analysis is used as a reference to study the kinematics of the bearing outer/inner race faults of the IMS experimental datasets. Here we aim to employ the enhanced envelope spectrum calculated from the OFCMCoh [41]. The EES is calculated by integrating the OFCMCoh over the full spectral frequency band $\{f_{bw}; f_c\} = \{10240 \text{ Hz}; 5120 \text{ Hz}\}$. The OFCMCoh-EES for bearing outer race fault (Set No.2) is computed and displayed in Fig. 9.

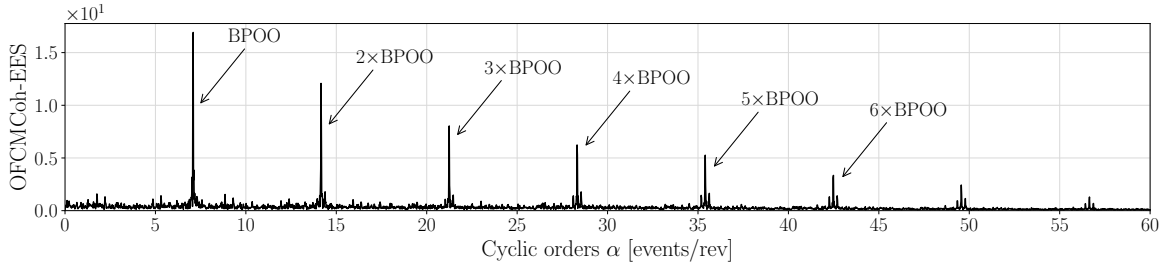

Figure 9: OFCMCoh-EES applied on the measurement number 703 of bearing 1 with bearing outer race fault.

As expected, the bearing outer race fault with BPOO of approximately 7.08 orders of the shaft speed is prominent on the OFCMCoh-EES. This result also suffices to show, in a general way, the order-frequency analysis is powerful in disclosing the hidden cyclic periodicities. The presence of multiple harmonics and sidebands related to the cage modulation indicates that the effect of the bearing slip on the repetitive transients was minimal. In general, both the AT-IPS-based cyclomap (see Fig. 6(b)) and the OFCMCoh-EES were able to detect the bearing outer race fault. However, the AT-IPS-based cyclomap presents richer diagnostic information related to the phase angle of each repetitive transient.

The OFCMCoh-EES for bearing outer race fault (Set No.3) with BPOO of approximately 7.10 orders of the shaft speed is computed and displayed in Fig. 10. This envelope spectrum is apparently very similar to the previous results, thus indicating the outer race fault with cage modulation (i.e. small sidebands around the BPOO). As a practical matter, however, the spectral analysis rests heavily on the assumption that the vibration signal to be analysed is strictly CS, but when this is not the case, we are confronted with a much more difficult problem associated with *smearing phenomena*: serious departures from the basic assumption of periodicity can result in the loss of diagnostic information on the spectrum [3]. However, most CS2 tools if not all still perform effectively for bearing diagnostics under a stationary regime because the pseudo-CS signal is not associated with severe distortions.

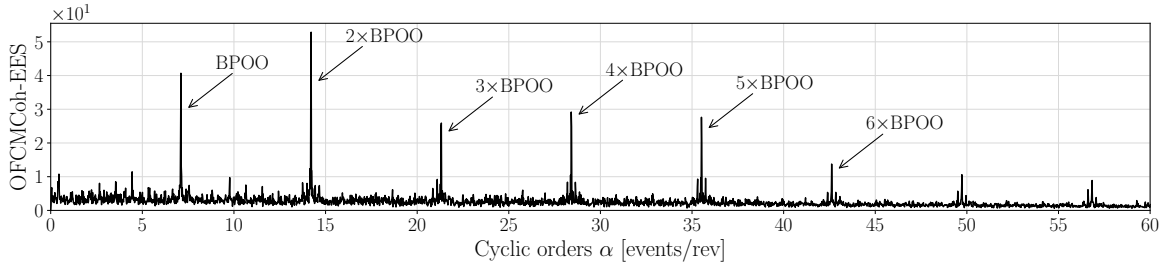

Figure 10: OFCMCoh-EES applied on the measurement number 6316 of bearing 3 with bearing outer race fault.

It behooves us equally to consider the possible disadvantages of this phase-cycle analysis as an alternate approach to fault diagnostics. Perhaps the greatest of these is these is the prior knowledge of the fault period with sufficient precision. While the order-frequency analysis estimates the spectral density to disclose the hidden cyclic modulations, the phase-cycle analysis uses only the spectral components. This renders it quite ineffective as a detector of hidden cyclic modulations.

The OFCMCoh-EES for bearing inner race fault (Set No.1) with BPOI of approximately 2.02 orders of the shaft speed is computed and displayed in Fig. 11. In this case, the OFCMCoh-EES failed to diagnose the bearing inner race fault because some spurious harmonics were observed. In particular, we cannot distinguish the fault because of the nature of harmornics that appear at every cyclic orders α. Similarly, the cyclomap in Fig. 8(b) failed to diagnose the inner race fault. To conclude, the OFCMCoh-EES is a powerful tool in bearing diagnostics because of its advanced performance in disclosing hidden cyclic periodicities.

4.2. C-AIM experimental dataset

In the last section, we showed the kinematics of the bearing inner and outer race faults. This section is devoted to studying the fault signature of the localised gear fault and the strong interference. The interference resembles the bearing outer race fault and can

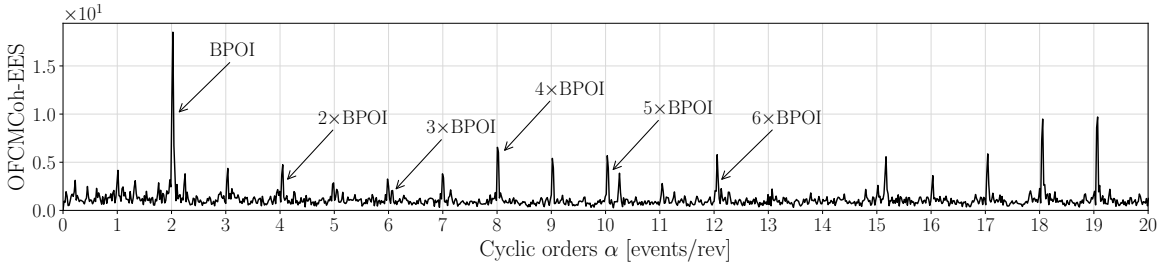

Figure 11: OFCMCoh-EES applied on the measurement number 2156 of bearing 3 with bearing inner race fault.

be used to obtain insight into diagnosing bearing damage under non-stationary conditions. In practical applications, many types of rotating machinery such as gearbox systems are exposed to various operating condition regimes that degrade the gears and bearings. The aim of this section is to study the kinematics of localised gear fault using the AT-IPS-based cyclomap and to understand the behaviour of the strong interference component that impedes gear damage.

The run-to-failure data of the gear provided by the Centre for Asset Integrity Management (C-AIM) at the University of Pretoria in South Africa are used as a benchmark dataset. The helical gearbox test rig was originally designed by Stander and Heyns in Ref. [71]. It mainly consists of an alternator, three helical gearboxes, and an electrical motor. The test rig also consists of a set of vibration acquisition systems, a personal computer, and a control box that cannot be seen in the setup. The two helical gearboxes which are not monitored have the same structure, the one connected with the motor reduces speed and the other one increases speed. The monitored helical gearbox is comprised of bearings, gear, pinion, and shafts. An alternator and electrical motor apply time-varying load and speed to the test rig respectively. The C-AIM experimental test rig is shown in Fig. 12.

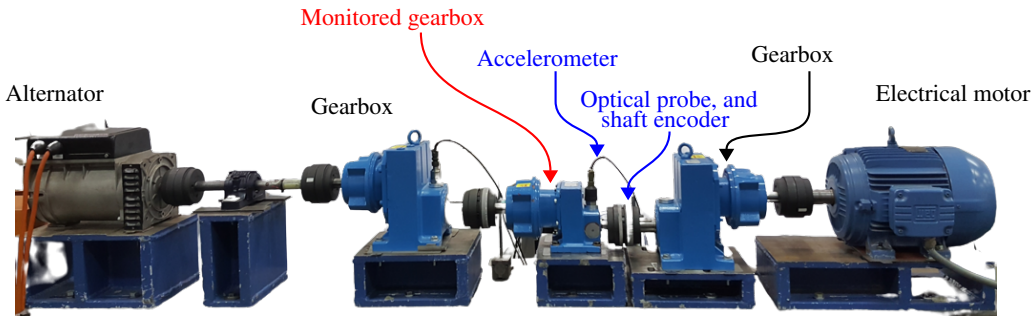

Figure 12: Centre for Asset Integrity Management (C-AIM) experimental test rig [72].

The monitored helical gearbox on the C-AIM experimental test rig is Siemens E68-A-100 helical gearbox, and the other two gearboxes are Siemens E38-A-100 helical gearboxes. The motor is Weg 5,5 kW three-phase four-pole squirrel cage electrical motor, and the alternator is a 5.5 kVA Mecc Alte spa three-phase alternator. Two accelerometers were used to measure the vibration signals on the monitored gearbox. The first accelerometer is the Wilcoxon ICP uni-axial accelerometer, which is mounted on top of the gearbox casing. The second accelerometer is a 100 mV/g PCB ICP tri-axial accelerometer which cannot be seen in the setup, it is mounted on the side of the gearbox casing.

In a helical gearbox system, the pinion and gear teeth are prone to local faults including root cracks, tooth wear, chipped tooth, and broken teeth because they experience high load due to harsh environmental conditions. For these reasons, a root crack on the gear tooth located in the monitored gearbox is created in our experiments. The gear has 37 teeth and the pinion has 20 teeth, and thus the gear ratio of the helical gearbox is $37/20 = 1.85$. The gear before and after the fatigue experiment is shown by a cracked and broken tooth, which is illustrated in Fig. 13. An eight-channel OROS OR35 data acquisition system is used to acquire the vibration signal for further processing.

The instantaneous angular speed displayed in Fig. 14 in was estimated from a zebra-tape shaft encoder with 88 pulses per revolution and Optel Thevon optical switch. The vibration signals were collected under varying load and speed conditions. The sampling frequency Δ_f is 25.6 kHz, and the sampling length is almost 20 sec. A sampling frequency Δ_f of 51.2 kHz is used for the Optel Thevon optical switch to capture the shaft position accurately on the Zebra-strip shaft encoder. During the fatigue experiment, a total of 1400 files were collected. However, only 200 files ranging from files 1 to 1400 with equal spacing will be used to capture the damage signal from inception to completion of this experiment.

The instantaneous angular speed ranging between 13 to 18 rad/s is imposed on the motor to represent the time-varying operating

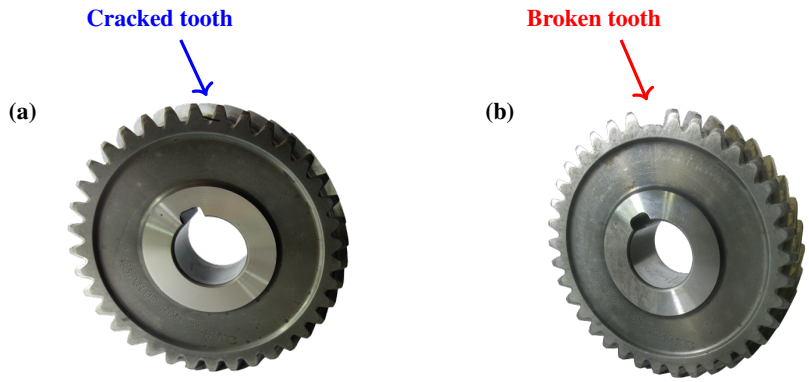

Figure 13: Helical gear in the C-AIM experimental test rig (a) gear with 50% cracked tooth representing incipient fault, and (b) gear with broken tooth representing matured fault [72].

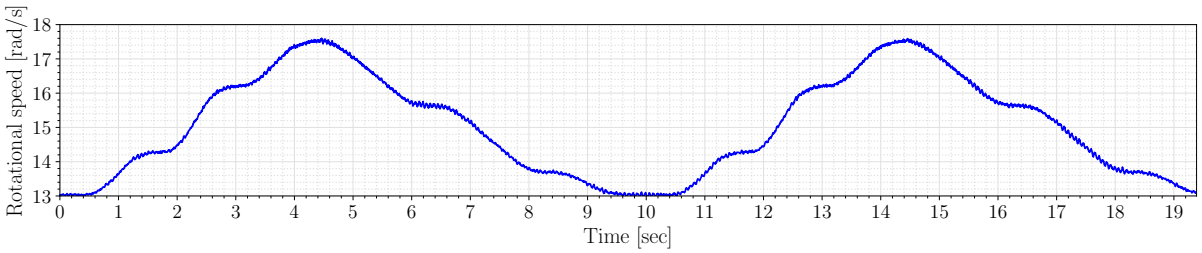

Figure 14: The instantaneous angular speed for C-AIM experimental test rig.

conditions. This operating condition provides sufficient complexity to critically evaluate the performance of the proposed methods in diagnosing the gear fault with low-impact energy. The time-varying operating conditions are expected to cause both amplitude and phase modulation on the measured vibration signal. As a result, the measured vibration signal of gear faults is often a mixture of the *first-order cyclo-non-stationary* (CNS1) signals [73], background noise, and *second-order cyclo-non-stationary* (CNS2) signals.

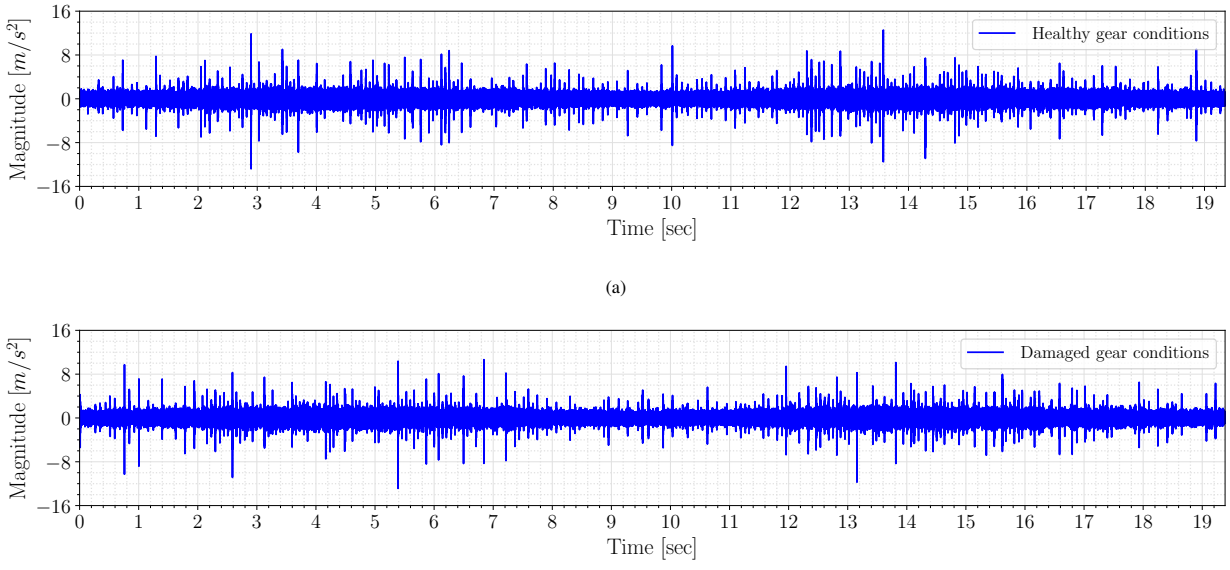

Figure 15: Acceleration signals acquired from the helical gearbox casing (a) healthy gear conditions, and (b) damaged gear conditions.

The Acceleration signals acquired from the helical gearbox casing illustrated in Fig. 15(a) and 15(b) represent the healthy gear conditions (measurement number 1) and damaged gear conditions (measurement number 6) respectively. Looking at the measured

vibration signals, it is not possible to conclusively identify the localised gear fault. This vibration signal is heavily clouded by strong interference with substantially large magnitudes. This interference appears on both vibration signals with healthy gear conditions and damaged gear conditions. This impedes the application of many conventional signal-processing techniques. In the next section, we study the kinematics of the first-order cyclo-non-stationary signals (i.e. a deterministic part of CNS signal) which are known to mask the gear and bearing fault signatures of the gearbox system under non-stationary conditions.

4.2.1. Deterministic gear components

There are, however, many phenomena intimately connected with the measured vibration signal from the gearbox system. Often, the deterministic gear components dominate the vibration response. It is almost impossible to perform gear and bearing diagnostics of the gearbox system without being confronted by strong deterministic gear components. The deterministic gear components are sources of conceptual complication that can lead to complications in practice, including erroneous procedures and misinterpretation of results. They professed to be localised faults, however, phenomena of this kind are of everyday occurrence in the gearbox system, and may generally not reflect the conditions of gears. It is therefore important to detect damage despite the impeding signal components.

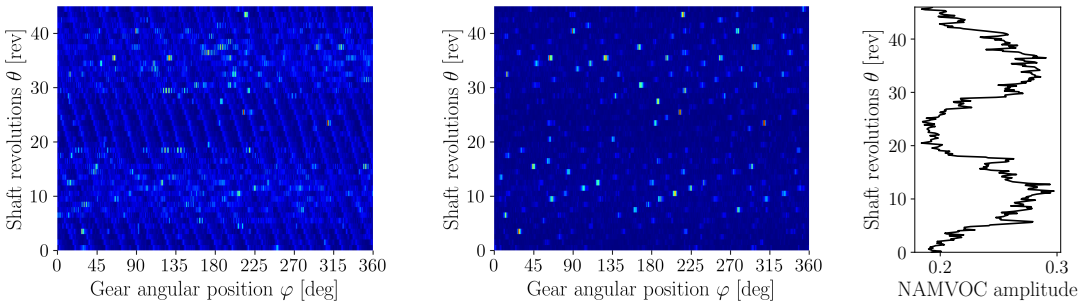

(a) Before cepstrum pre-whitening (b) After cepstrum pre-whitening (c) Modulations

Figure 16: Helical gearbox measured vibration signal (measurement number 1) with healthy gear conditions (a) AT-IPS-based cyclomaps, showing deterministic gear components before applying cepstrum pre-whitening, (b) AT-IPS-based cyclomaps for cepstrum pre-whitened signal with strong impulsive interferences, and (c) NAMVOC amplitude modulations for raw signal.

Illustrated in Fig. 16(a) is the cyclomap for the acceleration signal acquired from the helical gearbox casing with healthy gear conditions (see Fig. 15(a)), occurring at an angular period of $\Delta\theta = \phi = \alpha_{fault}^{-1} = 1$ rev. In this case, the total number of points on the cyclomap scales almost as $L_\varphi L_\theta \sim 2^{14.097}$, (i.e. $\{L_\varphi; L_\theta\} = \{381; 46\}$) when the minimum angular speed difference is calculated as $\Delta\vartheta_{rev}^{(min)} = 8.063 \times 10^{-5}$, the total number of shaft revolutions is $\vartheta_{rev}[L_t - 1] = 46.4658$ rev, the window length is $N_w = 2^7$, and the overlap fraction is $R_o = 0.75$. CPW is used to remove deterministic components before diagnosing the gear and bearing faults [63].

The CPW is capable of attenuating deterministic gear components for much wider applications blindly. Hence, using this simple approach is by no means difficult to attenuate deterministic gear components. The simplicity of the CPW caused the traditional method for attenuating deterministic gear components to be generally superseded by far since it is very easy to implement with no unknown parameters to be determined. After applying the CPW, the random part of the vibration signal which usually contains fault-related signals and background noise is preserved as illustrated in Fig. 16(b). In this case, the random interference survived the CPW. Additional processing needs to be performed to filter out the interference.

A standard procedure to remove the CNS1 signals such as deterministic gear components under a non-stationary regime is by first removing the amplitude modulation (see Fig. 16(c)) using NAMVOC, then apply the CPW. This approach enforces the CNS1 signals related to deterministic components to behave like CS1 signals. Then the CPW can effectively attenuate the CS1 signals. Our aim is first to ascertain the nature of deterministic gear components and then to find out how the time-varying operating condition contributes to amplitude and phase modulations. The filtered deterministic gear components are presented in Fig. 17 as a demonstration of the described phenomenon. The deterministic gear components experience strong amplitude modulations.

The object of showing the zoomed-in view of the obvious and hidden periodicities (see Figs. 17(b) and 17(c)) of the deterministic gear components are only to give a rough idea to the reader of the nature with which these deterministic components manifest themselves in practice. In this case, the obvious periodicities do not show any perceptible amplitude modulations as compared to hidden periodicities. An elemental feature of any obvious periodicities forms a complete sequence that tends to recur over and over again at more or less regular intervals of time or in amplitude. This is because phenomena in the time domain are rarely periodic. In fact, when examined under a microscope, no known phenomenon is precisely periodic, just as waves following each other on the sea do not repeat each other perfectly. In the case of hidden periodicities, the strength of the sinusoidal waves in the vibration signal is

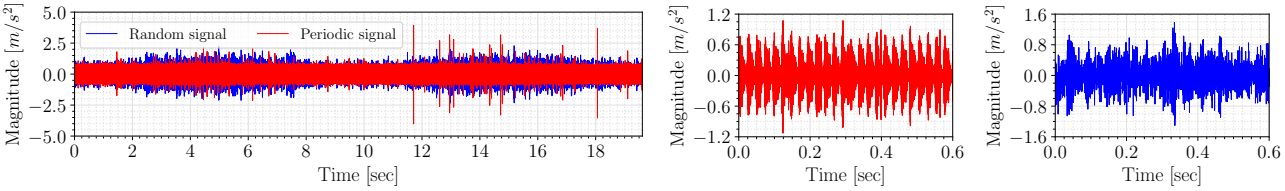

(a) Filtered deterministic gear component signals

(b) Obvious periodicities

(c) Hidden periodicities

Figure 17: Deterministic gear components for helical gearbox measured vibration signal (measurement number 1) with healthy gear conditions, (a) Random and periodic signals at the spectral frequency of approximately 1.2 and 8 kHz respectively, (b) Zoomed-in view of the periodic signal in the range [0, 0.6] sec, and (c) Zoomed-in view of the random signal in the range [0, 0.6] sec.

weak relative to the background noise. The cyclomaps for deterministic gear components with obvious and hidden periodicities are presented in Figs. 18(a) and 18(b) respectively.

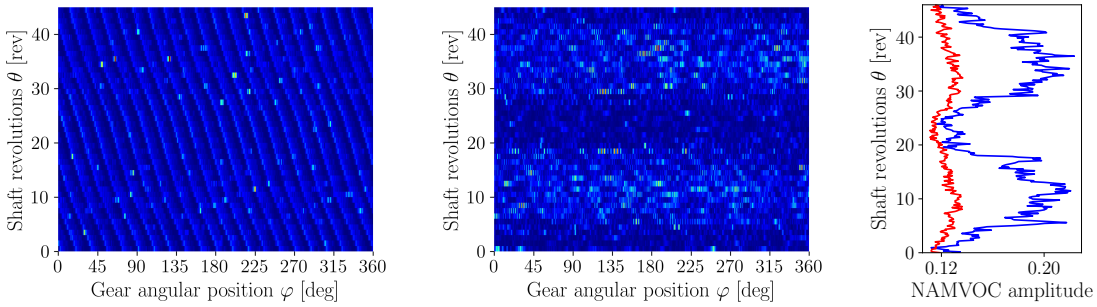

(a) Obvious periodicities

(b) Hidden periodicities

(c) Modulations

Figure 18: Deterministic gear components for helical gearbox measured vibration signal (measurement number 1) representing first-order cyclo-non-stationary signals, (a) Periodic signal at a spectral frequency of 8 kHz, (b) Random signal at a spectral frequency of 1.2 kHz, and (c) NAMVOC amplitude modulations: (i) periodic signal (red continuous line), and (ii) random signal (blue continuous line).

The kinematical properties of the deterministic gear components with hidden periodicities furnish no true insight into the nature of the signal. The manner of the deterministic gear components and consequent amplitude modulations (see Fig. 18(c)) vary slightly from point to point due to non-stationary operating conditions. In this way, the idea of NAMVOC to remove amplitude modulations is seen to be justified, and we may properly say that it will improve the performance of the CPW. The object of this section was to show the kinematics of the deterministic gear components. We have therefore obtained the nature of the deterministic gear components on the cyclomaps which will enable us to explain how they impede the detection of the localised gear fault in a subsequent subsection.

4.2.2. Localised gear fault

The preceding results proved conclusively that the gearbox system produces strong deterministic gear components that usually impede the detection of local faults. In this subsection, the kinematics of the localised gear fault are examined more thoroughly than has yet been done. In most practical situations, the assumption of stationary operating conditions is nonexistent, especially for wind turbines. This is worthy of mention here, even though we cannot take the space to describe it in detail. As a result, the application of NAMVOC to remove amplitude modulation is imperative in gear and bearing diagnostics. Many of the practical problems one encounters in connection with the amplitude modulations are well treated by Schmidt and Heyns in Ref. [62]. The phase-cycle analysis makes it possible to observe the underlying characteristics of the signal, and the results already achieved permit the hope that an accurate diagnostic conclusion can be drawn. Illustrated in Fig. 19 is the cyclomaps for the acceleration signal acquired from the helical gearbox casing with damaged gear conditions (see Fig. 15(b)).

In the first instance, the cyclomap is applied to the raw signal (see Fig. 19(a)) with the expectation of eliciting the repetitive transients of the localised gear fault. However, in this case, the repetitive transients of the localised gear fault are not observed. In general, the kinematical properties of many types of rotating machinery such as gearbox systems are very complicated because they involve a complicated interplay between the nature of the defects and environmental factors. It is fair to say that the deterministic gear components with random periodicity are dominating in this representation of the cyclomap. Hence, extreme caution is imperative when drawing conclusions about the conditions of the localised gear fault using the raw signal in Fig. 19(a).

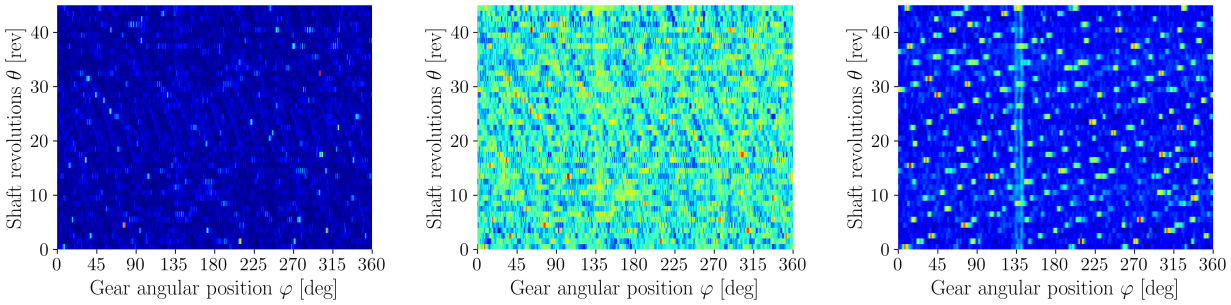

(a) Raw signal (b) Logarithmic scale (c) Whitened signal + logarithmic scale

Figure 19: Gearbox measured vibration signal (measurement number 6) with localised gear fault at an angular position of 135 deg, occurring at an angular period of $\Delta\theta = \phi = \alpha_{fault}^{-1} = 1$ rev, using the AT-IPS-based cyclomaps, $\varepsilon_x^{\phi;\Delta\tau}(\varphi;\theta,\Delta\theta)$, for (a) raw vibration signal, (b) raw vibration signal and cyclomap in logarithmic scale, and (c) whitened vibration signal and cyclomap in logarithmic scale.

In the second instance, we investigated whether the use of a logarithmic scale on the cyclomap for the raw signal can improve the detection of a localised gear fault. An illustration of the cyclomap in logarithmic scale is provided in Fig. 19(b). Neither the cyclomap of the raw signal nor the logarithmic scale gave any evidence of the localised gear fault. This representation of a raw signal on a logarithmic scale seems to involve so much obscurity. The use of a logarithmic scale may however lead to the inclusion of weak localised gear fault which had previously not revealed itself, if and only if the raw signal is whitened. As a result, the signal must be whitened first before we can draw conclusions about the conditions of the localised gear fault which subsists in the presence of deterministic gear components and strong interferences. This approach is expected to admit to easy comparison since the potential difference before and after applying the logarithmic scale to raw signal are very nearly the same. Lastly, the logarithmic scale cyclomap of the whitened signal is computed and displayed Fig. 19(c) in order to enhance the detection of weak localised gear fault occurring at an angular position of approximately 135 deg.

In this case, the detection of the localised gear fault improved after applying CPW, but the most decisive improvement occurred when the logarithmic scale was used. We can without much difficulty deduce, not only the repetitive transients of the interference but also the localised gear fault which is phase-locked to an angular position of approximately 135 deg. Of course, the repetitive transients of the localised gear fault are heavily clouded by the interference and the necessity of using the informative frequency band methods to increase the SNR confronts us. One major property of AT-CS signals is that they can be isolated from compound faults with ease, allowing the detection of weak defects hidden in high levels of background noise. In general, the employment of phase-cycle analysis in the detection of gear and bearing faults is, like all methods of analysis, subject to definite limitations which must be clearly borne in mind, otherwise, faulty interpretations are likely to be made. When heavy Gaussian noise or strong interferences has been found to offer insuperable difficulties even after filtering the vibration signal, it seems to be equally natural to discard the phase-cycle analysis, unless something more than a mere trace of gear or bearing fault can be detected.

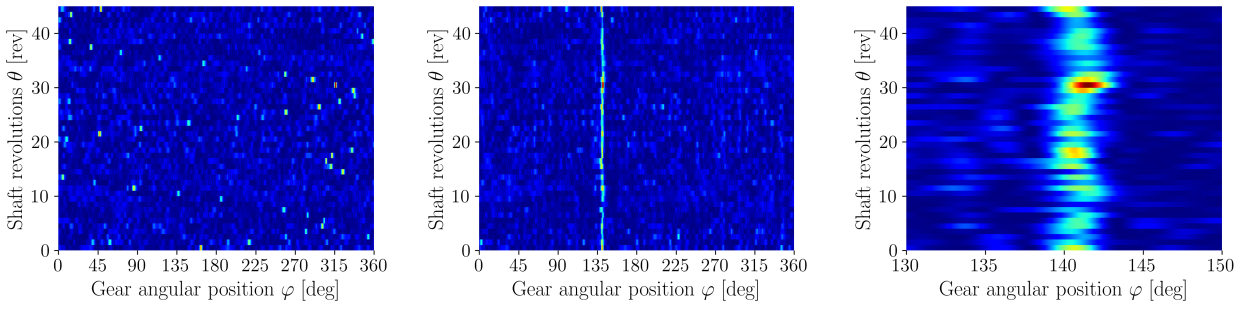

(a) Before angular resampling (b) After angular resampling (c) Zoomed-in view (After angular resampling)

Figure 20: Localised gear fault (measurement number 6) representing second-order cyclo-non-stationary signal, (a) before angular resampling, (b) after angular resampling, and (d) zoomed angular position in the range [130-150] deg after performing angular resampling.

The cyclomap for the CNS2 signal is presented in Fig. 20(a) as a demonstration of the phase modulations associated with a non-stationary regime. In this case, we used an optimal filter band of $\{f_{bw}; f_c\} = \{200\text{ Hz}; 500\text{ Hz}\}$, identified using the IFBI$_a$gram [74, 75] to enhance the detection of the localised gear fault that is essentially bandlimited. The object is to disclose repetitive transients generated by early gear fault from helical gearbox casing vibration signal before performing angular resampling. From

the preceding results, it can be seen that the repetitive transients undergo a remarkable transformation due to phase modulations and appear to become *completely incoherent*. However, in practical applications, we do not, and almost always should not, use this cyclomap for gear and bearing diagnostics in the presence of time-varying operating conditions because the distortion due to phase modulations are more grievous to repetitive transients than imprecise angular period. Even when this representation is used, however, it will rarely show the kind and location of the fault, and hence we cannot draw valid diagnostic conclusions.

After performing angular resampling, the CNS2 signal returned to some semblance of the CS2 signal as illustrated in Fig. 20(b). The gear teeth are presumed healthy on the gear angular position with minimum amplitude. The cyclomap provides very detailed and accurate information about the repetitive transients which leaves no doubt that the localised gear fault has occurred at an angular position of approximately 135 deg. In practice, many gear faults including fatigue cracks or spalls on a tooth face, are localised. Therefore, their angular position is very short as compared with the angular position for one complete revolution of the gear. In this case, all the CS2 tools which have long been recognised as effective tools for machine condition monitoring will perform optimally in diagnosing the fault. Since the length of the shaft revolutions θ on the cyclomap at an angular period of interest gives information about the total number of repetitive transients, this localised gear fault has 46 repetitive transients. We have repeatedly stressed in previous subsections that it is essential to know the precise angular period *à priori* because it controls the appearance of the repetitive transients and also the shaft revolutions resolution.

In order to deduce more detailed repetitive transients after performing the angular resampling, we zoomed the results around the localised gear faults (see Fig. 20(c)). This evidence indicates decisively that the angular resampling removed the phase modulations to a certain extent but not completely due to the inaccuracy of the estimated instantaneous angular speed (see Fig. 14) that was measured using the zebra tape shaft encoder with 88 pulses per revolution. This signal display CNS2 properties on the cyclomap because of the non-stationary repetitive transients with a microscopic variance of 0-3 deg. It is apparent that the angular resampling introduced infinitesimal error to repetitive transients of the localised gear fault. Perhaps this is not a matter of surprise when we consider that the estimated rotational speed is at best not very precisely determined. Probably in all cases, the phase-cycle analysis will enable us to reach qualitative if not accurate quantitative experimental deductions.

4.2.3. Interference

The phase-cycle analysis conforms generally to our intuitive ideas, and it enables us to classify a variety of signals and to describe their kinematical properties in a way that furnishes meanings for accurate diagnostic conclusions. In the previous section, we have successfully diagnosed the CNS2 signal and also showed the nature of the signal after performing angular resampling. The object of this section is to show the kinematical properties of the strong interference. The interference resembles the bearing outer race fault of the IMS experimental datasets and can be used to obtain insight into diagnosing bearing damage under non-stationary conditions. The cyclomaps for the acceleration signal acquired from the helical gearbox casing with damaged gear conditions are computed at an angular period of $\phi = \alpha^{-1} = 1/5.72$ rev, and displayed in Fig. 21. In this case, the total number of points on the cyclomap scales almost as $L_\varphi L_\theta \sim 2^{15.407}$, (i.e. $\{L_\varphi; L_\theta\} = \{164; 265\}$) when the minimum angular speed difference is calculated as $\Delta\vartheta_{rev}^{(min)} = 8.063 \times 10^{-5}$, the total number of shaft revolutions is $\vartheta_{rev}[L_t - 1] = 46.4658$ rev, the window length is $N_w = 2^7$, and the overlap fraction is $R_o = 0.90$.

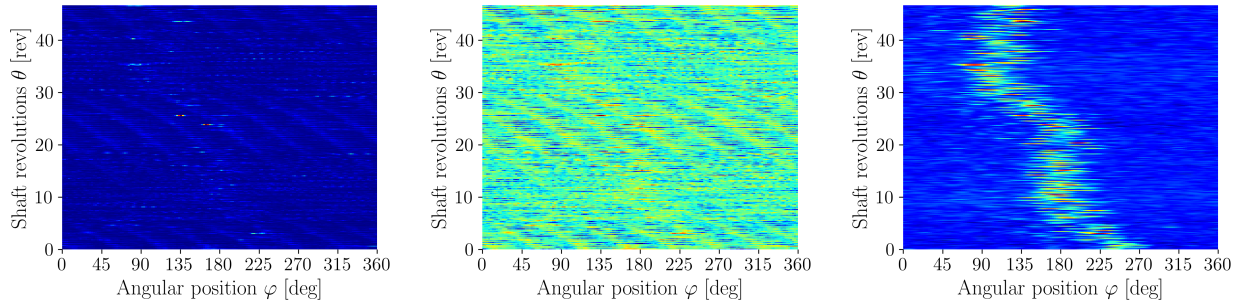

(a) Raw signal (b) Logarithmic scale (c) Whitened signal + logarithmic scale

Figure 21: Gearbox measured vibration signal (measurement number 6) with interference at a mean angular position of 175 deg, with 265 repetitive transients occurring at an angular period of $\Delta\theta = \phi = \alpha^{-1} = 1/5.72$ rev, using the AT-IPS-based cyclomaps, $\varepsilon_x^{\phi;\Delta\tau}(\varphi; \theta, \Delta\theta)$, for (a) raw vibration signal, (b) raw vibration signal and cyclomap in logarithmic scale, and (c) whitened vibration signal and cyclomap in logarithmic scale.

As expected, neither the cyclomap of the raw signal (see Fig. 21(a)) nor the logarithmic scale (see Fig. 21(b)) gave any evidence of the nature of the interference. In many practical applications, it is very rare to have a situation in which the measured vibration signal from the gearbox system is not heavily clouded by deterministic gear components. Therefore, we have to deal with deterministic gear components before we can diagnose a fault. Hence, logarithmic scale cyclomap of the whitened signal is computed and displayed Fig.

21(c) in order to enhance the detection of the interference because the magnitude of the repetitive transients varies proportionally with the non-stationary operating conditions. From the preceding results, it can be seen that the randomness caused by the interference is not large enough. It was, therefore, inferred that the large phase deviation in shaft revolutions θ range [0-10] and [22-32] rev must be caused by the errors after performing angular resampling. This can be explained since the angular resampling removed the phase modulations to a certain extent but not completely due to the inaccuracy of the estimated instantaneous angular speed. This problem is inveterately attached to rotational speed estimation using the zebra tape shaft encoder.

This interference was attributed to the contact made between a floating bearing and the casing of the gearbox when axial loads are applied on the shaft [2]. In general, the interference causes dominating repetitive transients that effectually obscure the localised gear fault on the measured vibration signal (see Fig. 15). To conclude, this section presented a new phase-cycle analysis within the AT-CS framework, which is therefore potentially of very widespread applicability. Based on the evidence, we believe that the phase-cycle analysis theory has considerable potential for rotating machines because of the kinematical properties that can be used to diagnose a variety of faults under different conditions.

4.2.4. OFCMCoh: Improved envelope spectrum

In this section, the acceleration signal acquired from the helical gearbox casing with damaged gear conditions will be scrutinised through the OFCMCoh for the sake of comparison. The OFCMCoh is the most powerful technique for CS2 signal detection which decomposes vibration signal into cyclic orders α and spectral frequency f. In the literature, the CS2 signals are known to exhibit spectral correlation without introducing any smearing phenomenon on the hidden cyclic modulations. The OFCMCoh for measurement number 6 and 200 is computed and displayed in Figs. 22(a) and 22(b).

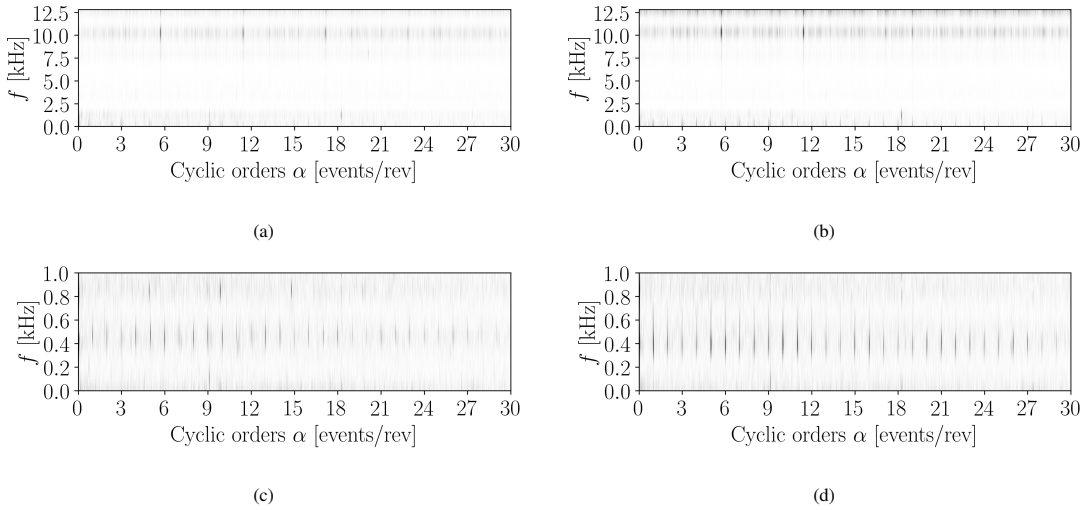

Figure 22: OFCMCoh for localised gear fault on (a) measurement number 6, (b) measurement number 200, (c) measurement number 6: zoomed-in view in spectral frequency f range [0-1] kHz, and (d) measurement number 200: zoomed-in view in spectral frequency f range [0-1] kHz.

The OFCMCoh of the measured vibration signal with localised gear fault can only unveil the strong interference signature at about 10.4 kHz. The excerpts of the OFCMCoh in spectral frequency f range [0-1] kHz are shown in Figs. 22(c) and 22(d). The OFCMCoh shows the presence of the localised gear fault with weak signatures. These OFCMCoh are able to show 30 harmonics of the localised gear fault in the spectral frequency of 0.5 kHz. Similar detection was much more difficult with the OFCMCoh displayed in Figs. 22(a) and 22(b).

In many cases, the OFCMCoh is difficult to interpret, so it is interesting to reduce it to a one-dimensional representation by projecting the surface over the cyclic orders α axis. Hence, the OFCMCoh-EES is computed by integrating the OFCMCoh over a full spectral frequency band of $\{f_{bw}; f_c\} = \{12800\text{ Hz}; 6400\text{ Hz}\}$ as illustrated in Fig. 23.

The first three harmonics of the strong interference can be identified in the OFCMCoh-EES. However, the harmonics of the localised gear fault are barely visible and are highly contaminated by strong interference. As mentioned earlier, this interference resembles outer race bearing fault under non-stationary conditions and we have successfully diagnosed it using the cyclomap in Section 4.2.3. This result also suffices to show, in a general way, how the non-stationary regime leads to the loss of diagnostic information in bearing diagnostics. The OFCMCoh-EES is often simple and understandable. However, It has become clear that it is not quite adequate for the purpose of diagnosing the localised gear fault in this specific case. Here the problem is handled in quite a different, and very interesting, fashion, involving the use of the OFCMCoh-IES. The OFCMCoh-IES is computed by integrating the OFCMCoh over a specific spectral frequency band of $\{f_{bw}; f_c\} = \{200\text{ Hz}; 500\text{ Hz}\}$. The OFCMCoh-IES presented in Fig. 24 gives admirable results of the localised gear fault.

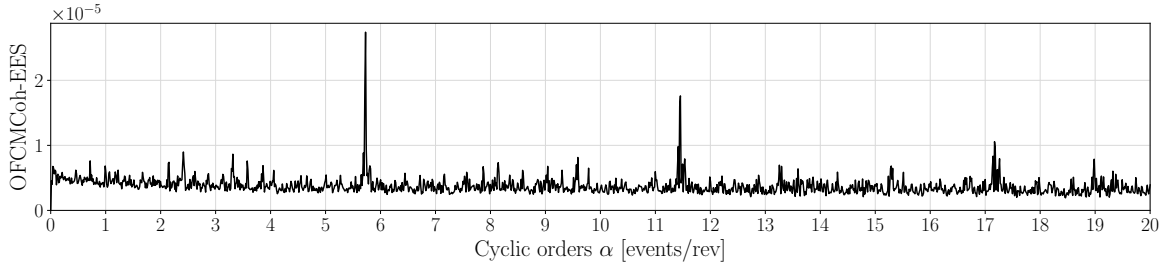

Figure 23: OFCMCoh-EES for localised gear fault in the full spectral frequency band, $\{f_{bw}; f_c\} = \{12800\text{ Hz}; 6400\text{ Hz}\}$.

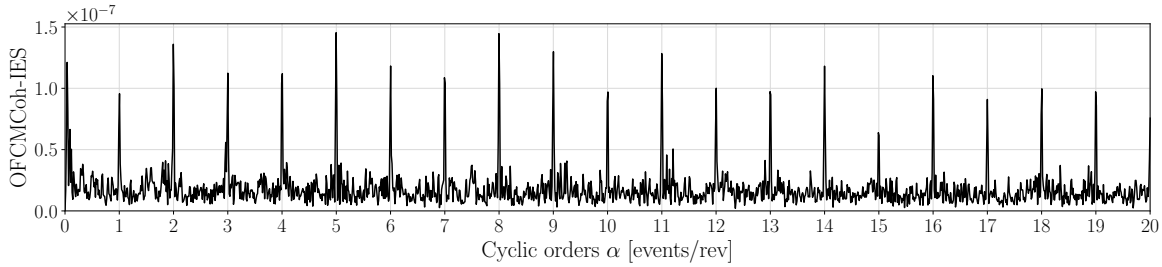

Figure 24: OFCMCoh-IES for localised gear fault in the optimal spectral frequency band, $\{f_{bw}; f_c\} = \{200\text{ Hz}; 500\text{ Hz}\}$.

When compared to the OFCMCoh-EES, the OFCMCoh-IES show higher performance in improving the SNR of the localised gear fault. Thus, spectral analysis based OFCMCoh-IES seems to improve the detection of CS2 signals when compared to the OFCMCoh-EES. In general, both the cyclomap (see Fig. 20) and the OFCMCoh-IES were able to detect the localised gear fault. However, the cyclomap present richer diagnostic information than the OFCMCoh-IES because we can also observe the errors introduced after performing angular resampling indicating that the the CNS2 signal returned to some semblance of the CS2 signal.

5. Conclusions

In this paper, the phase-cycle analysis using the theory of angle-time cyclostationary signals was proposed. The kinematics of gears and bearings under a variety of operating conditions were understood in terms of its cyclomap. At the same time, sufficient precision of the estimated angular period is necessary to avoid serious loss of diagnostic information about the gear and bearing conditions. The proposed cyclomap as a backbone of fault diagnostics was developed to identify the presence of the defect, its kind, its location, and it is based on the phase-cycle analysis. The techniques developed permit handling of special processing situations, in which the nature of repetitive transients is complex, such as the following: (i) phase modulation introduced after performing angular resampling, (ii) effect of cage modulations on the bearing outer race fault, and (iii) effect of the bearing slip on the periodicity of bearing fault. The method is computationally-effective which adds to its attractiveness.

The proposed method was successfully applied to the IMS (Intelligent Maintenance Systems) and C-AIM (Centre for Asset Integrity Management) experimental datasets. It worked for all cases in diagnosing bearing outer/inner race and localised gear faults which improved the decision-making process in understanding the cause of the fault and the factors that control its appearance. In practical application, this approach will lead to a better understanding of the meaning of the results of gear and bearing diagnostics by allowing the kinematical properties of different types of mechanical signals to be recognised and interpreted more precisely. However, in practice, the measured vibration signal usually provides more noise than the main source of faults. As a result, the detection of repetitive transients in the presence of strong background noises is a challenge. There's certainly plenty of room for improvement of phase-cycle analysis especially in the case of various noise sources.

Acknowledgements

The authors gratefully acknowledge the generous help of Professor J. Antoni. Our thanks to the referees for their constructive comments and valuable suggestions on the earlier version of the paper.

References

[1] D. Abboud, Y. Marnissi, A. Assoumane, Y. Hawwari, M. Elbadaoui, Synchronous analysis of cyclo-non-stationary signals: A comprehensive study with aeronautic applications, Mechanical Systems and Signal Processing 168 (2022) 108600.

[2] S. Schmidt, R. Zimroz, P. S. Heyns, Enhancing gearbox vibration signals under time-varying operating conditions by combining a whitening procedure and a synchronous processing method, Mechanical Systems and Signal Processing 156 (2021) 107668.

[3] R. B. Randall, J. Antoni, Rolling element bearing diagnostics—A tutorial, Mechanical Systems and Signal Processing 25 (2) (2011) 485–520.

[4] S. Schmidt, K. C. Gryllias, The anomalous and smoothed anomalous envelope spectra for rotating machine fault diagnosis, Mechanical Systems and Signal Processing 158 (2021) 107770.

[5] A. Mauricio, W. A. Smith, R. B. Randall, J. Antoni, K. C. Gryllias, Improved Envelope Spectrum via Feature Optimisation-gram (IESFOgram): A novel tool for rolling element bearing diagnostics under non-stationary operating conditions, Mechanical Systems and Signal Processing 144 (2020) 106891.

[6] A. Mauricio, K. C. Gryllias, Cyclostationary-based Multiband Envelope Spectra Extraction for bearing diagnostics: The Combined Improved Envelope Spectrum, Mechanical Systems and Signal Processing 149 (2021) 107150.

[7] J. Antoni, R. B. Randall, The spectral kurtosis: application to the vibratory surveillance and diagnostics of rotating machines, Mechanical Systems and Signal Processing 20 (2) (2006) 308–331.

[8] J. Antoni, The spectral kurtosis: a useful tool for characterising non-stationary signals, Mechanical Systems and Signal Processing 20 (2) (2006) 282–307.

[9] B. Rayleigh, A. Schuster, On the determination of the ohm in absolute measure, Proceedings of the Royal Society of London 32 (1881) 104–141.

[10] A. Schuster, On the investigation of hidden periodicities with application to a supposed 26 day period of meteorological phenomena, Terrestrial Magnetism 3 (1) (1898) 13–41.

[11] A. Schuster, On the periodicities of sunspots, Philosophical Transactions of the Royal Society of London. Series A, Containing Papers of a Mathematical or Physical Character 206 (1906) 69–100.

[12] A. Schuster, The periodogram and its optical analogy, Proceedings of the Royal Society of London. Series A, Containing Papers of a Mathematical and Physical Character 77 (515) (1906) 136–140.

[13] H. L. Trachtenberg, The analysis of the periodogram, Journal of the Royal Statistical Society 84 (4) (1921) 578–604.

[14] E. B. Wilson, Are there periods in american business activity?, Science 80 (2070) (1934) 193–199.

[15] E. Slutzky, The summation of random causes as the source of cyclic processes, Econometrica 5 (2) (1937) 105–146.

[16] M. G. Kendall, On the analysis of oscillatory time-series, Journal of the Royal Statistical Society 108 (1/2) (1945) 93–141.

[17] Z. A. Lomnicki, S. K. Zaremba, On estimating the spectral density function of a stochastic process, Journal of the Royal Statistical Society. Series B (Methodological) 19 (1) (1957) 13–37.

[18] E. Parzen, On consistent estimates of the spectrum of a stationary time series, The Annals of Mathematical Statistics 28 (2) (1957) 329–348.

[19] R. B. Blackman, J. W. Tukey, The measurement of power spectra from the point of view of communications engineering — Part I, The Bell System Technical Journal 37 (1) (1958) 185–282.

[20] R. B. Blackman, J. W. Tukey, The measurement of power spectra from the point of view of communications engineering — Part II, The Bell System Technical Journal 37 (2) (1958) 485–569.

[21] J. W. Tukey, Discussion, emphasizing the connection between analysis of variance and spectrum analysis, Technometrics 3 (2) (1961) 191–219.

[22] J. W. Cooley, J. W. Tukey, An algorithm for the machine calculation of complex fourier series, Mathematics of Computation 19 (90) (1965) 297–301.

[23] R. H. Jones, A reappraisal of the periodogram in spectral analysis, Technometrics 7 (4) (1965) 531–542.

[24] C. Bingham, M. D. Godfrey, J. W. Tukey, Modern techniques of power spectrum estimation, IEEE Transactions on Audio and Electroacoustics 15 (2) (1967) 56–66.

[25] M. S. Bartlett, On the theoretical specification and sampling properties of autocorrelated time-series, Supplement to the Journal of the Royal Statistical Society 8 (1) (1946) 27–41.

[26] M. S. Bartlett, Periodogram analysis and continuous spectra, Biometrika 37 (1/2) (1950) 1–16.

[27] M. S. Bartlett, J. Medhi, On the efficiency of procedures for smoothing periodograms from time series with continuous spectra, Biometrika 42 (1/2) (1955) 143–150.

[28] P. Whittle, Curve and periodogram smoothing, Journal of the Royal Statistical Society. Series B (Methodological) 19 (1) (1957) 38–63.

[29] U. Grenander, Bandwidth and variance in estimation of the spectrum, Journal of the Royal Statistical Society. Series B (Methodological) 20 (1) (1958) 152–157.

[30] P. D. Welch, The use of fast fourier transform for the estimation of power spectra: A method based on time averaging over short, modified periodograms, IEEE Transactions on Audio and Electroacoustics 15 (2) (1967) 70–73.

[31] W. A. Gardner, The spectral correlation theory of cyclostationary time-series, Signal Processing 11 (1) (1986) 13–36.

[32] W. A. Gardner, Measurement of spectral correlation, IEEE Transactions on Acoustics, Speech, and Signal Processing 34 (5) (1986) 1111–1123.

[33] W. A. Gardner, Spectral Correlation of Modulated Signals: Part I - Analog Modulation, IEEE Transactions on Communications 35 (6) (1987) 584–594.

[34] W. A. Gardner, W. A. Brown, C. Chen, Spectral Correlation of Modulated Signals: Part II - Digital Modulation, IEEE Transactions on Communications 35 (6) (1987) 595–601.

[35] W. A. Gardner, W. A. Brown, Fraction-of-time probability for time-series that exhibit cyclostationarity, Signal Processing 23 (3) (1991) 273–292.

[36] W. A. Gardner, A. Napolitano, L. Paura, Cyclostationarity: Half a century of research, Signal Processing 86 (4) (2006) 639–697.

[37] W. R. Bennett, Statistics of regenerative digital transmission, The Bell System Technical Journal 37 (6) (1958) 1501–1542.

[38] C. Capdessus, M. Sidahmed, J. L. Lacoume, Cyclostationary processes: application in gear faults early diagnosis, Mechanical Systems and Signal Processing 14 (3) (2000) 371–385.

[39] R. Boustany, J. Antoni, Cyclic spectral analysis from the averaged cyclic periodogram, IFAC Proceedings Volumes 38 (1) (2005) 166–171.

[40] J. Antoni, Cyclic spectral analysis in practice, Mechanical Systems and Signal Processing 21 (2) (2007) 597–630.

[41] D. Abboud, J. Antoni, Order-frequency analysis of machine signals, Mechanical Systems and Signal Processing 87 (2017) 229–258.

[42] P. Borghesani, The envelope-based cyclic periodogram, Mechanical Systems and Signal Processing 58-59 (2015) 245–270.

[43] J. Antoni, Cyclostationarity by examples, Mechanical Systems and Signal Processing 23 (4) (2009) 987–1036.

[44] J. Antoni, Cyclic spectral analysis of rolling-element bearing signals: Facts and fictions, Journal of Sound and Vibration 304 (3-5) (2007) 497–529.

[45] P. Borghesani, W. Smith, R. Randall, J. Antoni, M. El Badaoui, Z. Peng, Bearing signal models and their effect on bearing diagnostics, Mechanical Systems and Signal Processing 174 (2022) 109077.

[46] J. J. Broderick, R. F. Burchill, H. L. Clark, Design and fabrication of prototype system for early warning of impending bearing failure, NASA CR 123717 (1972).

[47] P. D. McFadden, J. D. Smith, Model for the vibration produced by a single point defect in a rolling element bearing, Journal of Sound and Vibration 96 (1) (1984) 69–82.

[48] P. D. McFadden, J. D. Smith, Vibration monitoring of rolling element bearings by the high-frequency resonance technique — a review, Tribology International 17 (1) (1984) 3–10.

[49] P. D. McFadden, J. D. Smith, The vibration produced by multiple point defects in a rolling element bearing, Journal of Sound and Vibration 98 (2) (1985) 263–273.
[50] M. S. Darlow, R. H. Badgley, G. W. Hogg, Application of high frequency resonance techniques for bearing diagnostics in helicopter gearboxes, Technical Report, US Army Air Mobility Research and Development Laboratory (1974) 74–77.
[51] J. Antoni, The infogram: Entropic evidence of the signature of repetitive transients, Mechanical Systems and Signal Processing 74 (2016) 73–94.
[52] J. Urbanek, T. Barszcz, R. Zimroz, J. Antoni, Application of averaged instantaneous power spectrum for diagnostics of machinery operating under non-stationary operational conditions, Measurement 45 (7) (2012) 1782–1791.
[53] J. Urbanek, T. Barszcz, J. Antoni, Time–frequency approach to extraction of selected second-order cyclostationary vibration components for varying operational conditions, Measurement 46 (4) (2013) 1454–1463.
[54] A. Marsick, H. André, I. Khelf, Q. Leclère, J. Antoni, Restoring cyclostationarity of rolling element bearing signals from the instantaneous phase of their envelope, Mechanical Systems and Signal Processing 193 (2023) 110264.
[55] A. Raad, J. Antoni, M. Sidahmed, Indicators of cyclostationarity: Theory and application to gear fault monitoring, Mechanical Systems and Signal Processing 22 (3) (2008) 574–587.
[56] S. Schmidt, P. Heyns, J. de Villiers, A tacholess order tracking methodology based on a probabilistic approach to incorporate angular acceleration information into the maxima tracking process, Mechanical Systems and Signal Processing 100 (2018) 630–646.
[57] C. Peeters, Q. Leclère, J. Antoni, P. Lindahl, J. Donnal, S. Leeb, J. Helsen, Review and comparison of tacholess instantaneous speed estimation methods on experimental vibration data, Mechanical Systems and Signal Processing 129 (2019) 407–436.
[58] G. Xin, N. Hamzaoui, J. Antoni, Extraction of second-order cyclostationary sources by matching instantaneous power spectrum with stochastic model – application to wind turbine gearbox, Renewable Energy 147 (2020) 1739–1758.
[59] J. W. Cooley, P. A. W. Lewis, P. D. Welch, The fast Fourier transform algorithm: Programming considerations in the calculation of sine, cosine and Laplace transforms, Journal of Sound and Vibration 12 (3) (1970) 315–337.
[60] C. H. Page, Instantaneous power spectra, Journal of Applied Physics 23 (1) (1952) 103–106.
[61] P. Borghesani, P. Pennacchi, S. Chatterton, The relationship between kurtosis- and envelope-based indexes for the diagnostic of rolling element bearings, Mechanical Systems and Signal Processing 43 (1) (2014) 25–43.
[62] S. Schmidt, P. S. Heyns, Normalisation of the amplitude modulation caused by time-varying operating conditions for condition monitoring, Measurement 149 (2020) 106964.
[63] P. Borghesani, P. Pennacchi, R. B. Randall, N. Sawalhi, R. Ricci, Application of cepstrum pre-whitening for the diagnosis of bearing faults under variable speed conditions, Mechanical Systems and Signal Processing 36 (2) (2013) 370–384.
[64] H. Qiu, J. Lee, J. Lin, G. Yu, Wavelet filter-based weak signature detection method and its application on rolling element bearing prognostics, Journal of Sound and Vibration 289 (4-5) (2006) 1066–1090.
[65] P. D. McFadden, A revised model for the extraction of periodic waveforms by time domain averaging, Mechanical Systems and Signal Processing 1 (1) (1987) 83–95.
[66] P. D. McFadden, Determining the location of a fatigue crack in a gear from the phase of the change in the meshing vibration, Mechanical Systems and Signal Processing 2 (4) (1988) 403–409.
[67] P. D. McFadden, Interpolation techniques for time domain averaging of gear vibration, Mechanical Systems and Signal Processing 3 (1) (1989) 87–97.
[68] D. Abboud, M. Elbadaoui, W. A. Smith, R. B. Randall, Advanced bearing diagnostics: A comparative study of two powerful approaches, Mechanical Systems and Signal Processing 114 (2019) 604–627.
[69] C. Peeters, J. Antoni, J. Helsen, Blind filters based on envelope spectrum sparsity indicators for bearing and gear vibration-based condition monitoring, Mechanical Systems and Signal Processing 138 (2020) 106556.
[70] P. McFadden, Examination of a technique for the early detection of failure in gears by signal processing of the time domain average of the meshing vibration, Mechanical Systems and Signal Processing 1 (2) (1987) 173–183.
[71] C. J. Stander, P. S. Heyns, Instantaneous angular speed monitoring of gearboxes under non-cyclic stationary load conditions, Mechanical Systems and Signal Processing 19 (4) (2005) 817–835.
[72] D. H. Diamond, P. S. Heyns, A. J. Oberholster, Online shaft encoder geometry compensation for arbitrary shaft speed profiles using Bayesian regression, Mechanical Systems and Signal Processing 81 (2016) 402–418.
[73] D. Abboud, J. Antoni, S. Sieg-Zieba, M. Eltabach, Deterministic-random separation in nonstationary regime, Journal of Sound and Vibration 362 (2016) 305–326.
[74] S. Schmidt, A. Mauricio, P. S. Heyns, K. C. Gryllias, A methodology for identifying information rich frequency bands for diagnostics of mechanical components-of-interest under time-varying operating conditions, Mechanical Systems and Signal Processing 142 (2020) 106739.
[75] S. Schmidt, P. S. Heyns, K. C. Gryllias, An informative frequency band identification framework for gearbox fault diagnosis under time-varying operating conditions, Mechanical Systems and Signal Processing 158 (2021) 107771.